IPP-Report

Max-Planck-Institut
für Plasmaphysik

David Kaltenbrunner

On the effect of the toroidal field ripple on the MHD equilibria of DEMO

IPP 2022-04
März 2022

On the effect of the toroidal field ripple on the MHD equilibria of DEMO

Masterthesis vorgelegt von

David Kaltenbrunner

beim Fachbereich Physik der

Universität Konstanz

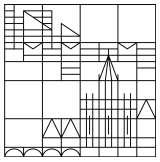

am 25. März 2022,

angefertigt am
Max-Planck-Institut für Plasmaphysik.

Erstgutachter: Prof. Dr. Gerd Ganteför

Zweitgutachter: Prof. Dr. Hartmut Zohm

Zusammenfassung

Das Ziel des **I**nternationalen **T**hermonuklearen **E**xperimentellen **R**eaktors (ITER) ist es zu zeigen, dass in einem Tokamak-Plasma mehr Energie freigesetzt werden kann, als zur Heizung benötigt wird. Das ist eine fundamentale Voraussetzung für zukünftige Fusionskraftwerke. ITER ist jedoch ein experimenteller Reaktor und wird keine Energie in das Stromnetz einspeisen. DEMO soll als europäischer Nachfolger von ITER ein Demonstrationskraftwerk werden und befindet sich in der Konzeptphase. Für ein zukünftiges Fusionskraftwerk kommen mehrere Bauformen in Frage, jedoch ist die experimentelle Grundlage für das Tokamak-Konzept die am weitesten fortgeschrittene. Die Bereitstellung von zusätzlichen Datenpunkten durch ITER in der Skalierung von Plasmaparametern machen das Tokamak-Konzept für DEMO attraktiv.

In der Theorie ist ein Tokamak-Plasma 2D durch die Achsensymmetrie um die Torusachse. In realen Tokamaks wird diese Symmetrie jedoch durch die endliche Anzahl an Toroidalfeldspulen gebrochen. Das Toroidalfeld hat eine räumliche Variation mit der Periodizität der Anzahl der Toroidalfeldspulen. Diese Variation wird toroidaler Feldrippel genannt. Sie ist eine 3D Störung und ermöglicht Effekte, die die Güte des Energieeinschlusses reduzieren. Diese sollte jedoch für ein wirtschaftlich attraktiven Fusionsreaktor maximal sein. Deshalb wird der Einfluss und die Reduktion des toroidalen Feldrippels in einem DEMO Tokamak untersucht. Als Teil dieser Untersuchungen werden **M**agneto**H**ydro**D**ynamische (MHD) Gleichgewichte in dieser Thesis betrachtet. Dafür werden Simulationscodes verknüpft, um die 3D Flussflächen in der statisch idealen MHD mittels Minimierung der Plasmaenergie durch variieren der Flussflächengeometrie zu berechnen. Für ein wohldefiniertes MHD-Problem werden das Druck- und Plasmastromprofil vorgeschrieben. Diese Profile werden durch vorhergehende Transportsimulationen bereitgestellt, zusammen mit der Geometrie des Plasmarands und dem gesamten toroidalen magnetischen Fluss. Der toroidale magnetische Fluss ist dabei eine Erhaltungsgröße, der Plasmarand jedoch wird variiert in 3D Simulationen zur Minimierung der Plasmaenergie. Für diese Simulationen wird ein 3D Vakuuminduktionsfeld benötigt, welches durch das Biot-Savart Gesetz bestimmt wird. Dieses wird angewendet auf Stromfäden, welche ein Spulensystem aus Toroidalfeldspulen, Poloidalfeldspulen und Transformator repräsentieren. Weiterhin werden ferromagnetische Einlagen in der Wand des Vakuumgefäßes durch ein Spulenmodell eingebunden, welches ihre die Reduzierung des toroidalen Feldrippels reproduzieren kann.

Das System aus Simulationscodes wird erfolgreich angewendet, um die Plasmareaktion auf den toroidalen Feldrippel für die neuesten DEMO baselines (2017-2019) zu berechnen. Die Plasmareaktion wird dabei für ein L-mode- und H-mode-Szenario durch die Amplitude der Flussflächenwellung untersucht. Der Bedarf für 3D Simulationen wird verdeutlicht durch ein Vergleich der Vakuumapproximation zu 3D Simulationen mit beweglichem Plasmarand. Dabei werden Abweichung zwischen 17 % und 26 % der Vakuumapproximation festgestellt. Weiterhin wird die Erwartung, dass der toroidale Feldrippel eine nicht resonante Störung ist, für beide Plasmaszenarien bestätigt. Dies wird erreicht durch einen direkten Vergleich des toroidalen Feldrippels des Vakuumfeldes und der Amplitude der Flussflächenwellung des Plasmas.

Abstract

The goal of the **I**nternational **T**hermonuclear **E**xperimantal **R**eactor (ITER) is to show, that inside a tokamak plasma more thermal fusion power can be released than it is needed for heating the plasma. This is a fundamental requirement for future fusion power plants. However, ITER is an experimental reactor and will not feed energy into the grid. Currently in the conceptual phase, DEMO is the European successor of ITER and is planned to be a demonstration fusion power plant. While several types of reactors are considered when building a fusion power plant, the experimental basis of the tokamak concept is considered the most advanced. Using the intermediate data points in the scaling of the plasma parameters, provided by ITER, makes a tokamak version of DEMO attractive.

In theory, a tokamak confines an axisymmetric 2D plasma around the major axis of the torus. However, in a real tokamak the finite number of toroidal field coils breaks this symmetry. The toroidal field has a spatial variation with a periodicity of the number of toroidal field coils. This variation is called the toroidal field ripple and is a 3D perturbation of a tokamak plasma. This gives rise to effects that reduce the energy confinement. Yet, to be economically successful, the energy confinement of a fusion reactor should be maximized. Thus, the effect and the reduction of the toroidal field ripple in a DEMO tokamak is investigated. As part of these investigations, the **M**agneto**H**ydro**D**ynamic (MHD) equilibria are considered in this thesis. Therefore, a simulation code system is coupled, computing 3D flux surfaces in the static ideal MHD equilibrium through minimization of the plasma energy by varying the geometry of the flux surfaces. For this to be a well-defined MHD problem, the pressure and plasma current profile are prescribed. These profiles are supplied from preceding turbulent transport simulations, together with the plasma boundary and the total toroidal magnetic flux. Whereas the toroidal magnetic flux is preserved, the plasma boundary evolves in 3D free-boundary simulations to minimize the energy. Thus, a 3D vacuum induction field confining the plasma needs to be provided for the simulations. This vacuum induction field is determined by applying the Biot-Savart law to current carrying filaments, representing the conductors of a coil system consisting of toroidal field coils, poloidal field coils and the central solenoid. Furthermore, to treat ferromagnetic inserts in the vacuum vessel wall by current carrying filaments a coil model, reproducing their reduction of the toroidal field ripple, is developed.

The newly coupled code system by is successfully applied to compute the plasma response to the toroidal field ripple for the latest DEMO baselines (2017-2019). The plasma response for a DEMO L-mode and H-mode is investigated by the amplitude of flux surface corrugation. The need for inherent 3D simulations is shown by a comparison between the vacuum approximation and a 3D free-boundary simulation. Deviations of 17 % to 26 % of the approximation to the 3D data is observed. Furthermore, the expected non-resonant perturbation of the toroidal field ripple is confirmed for the L-mode and for the H-mode. This is shown by direct comparison between the toroidal field ripple in the vacuum induction field and the plasma response, given by the amplitude of the flux surface corrugation.

Contents

1 Introduction

1.1 DEMO as a tokamak

As successor of the experimental fusion reactor ITER (**I**nternational **T**hermonuclear **E**xperimental **R**eactor), DEMO is supposed to be a fusion power plant feeding electrical energy into the grid in Europe. DEMO is planned to be a demonstration power plant (hence, the name DEMO) and achieving the transition of fusion reactors from an active field of research to an industry and technology oriented program [1]. For this transition many aspects need to be considered, e.g. maintainability, self sufficient fuel cycle and reactor safety. Besides these technological challenges, DEMO has to fulfill economical criteria to serve as solution for a realistic power plant in the future. A fundamental requirement is, that the released power inside the reactor is greater than the used power. The released energy inside a fusion reactor originates from fusion reactions of two nuclei to a single nucleus. The relevant fusion reaction for this thesis is that of the hydrogen isotopes Deuterium (D) and Tritium (T) according to

$$ {}^{2}_{1}\mathrm{D} + {}^{3}_{1}\mathrm{T} \longrightarrow {}^{4}_{2}\mathrm{He}(3.52\,\mathrm{MeV}) + {}^{1}_{0}\mathrm{n}(14.06\,\mathrm{MeV}) \Rightarrow Q_{fus} = 17.58\,\mathrm{MeV} \tag{1.1} $$

to a doubled charged α-particle ${}^{4}_{2}\mathrm{He}$ and an uncharged neutron ${}^{1}_{0}\mathrm{n}$, with a distributed energy release Q_{fus} of a single reaction [2]. In order for this reaction to take place with a considerable probability, the D-T mixture needs to be heated to the state of a plasma[1]. The criterion, that the released fusion power P_{fus} is greater than the heating power P_{heat}, can be expressed in terms of plasma parameters by the so-called Lawson criterion.

For the derivation of the Lawson-criterion the fusion power P_{fus} is given by

$$ P_{fus} = \frac{n}{2} \cdot \frac{n}{2} \langle \sigma v \rangle \cdot Q_{fus} \tag{1.2} $$

where it is assumed, that D and T ions are contained in the same densities inside the plasma and hence, both can be expressed as $n/2$. The middle term $n/2 \cdot \langle \sigma v \rangle$ is the probability per unit time for a fusion reaction, based on the reactivity $\langle \sigma v \rangle$ [2][2].

A further characteristic key figure for a fusion reactor is the energy confinement time τ_E, defined by

$$ \tau_E = \frac{(3/2)n(T_e + T_i)}{P_L + R} \left(= \frac{\text{confined energy}}{\text{total power loss}} \right) \tag{1.3} $$

[1] In the here presented work the confinement of this plasma in a external magnetic field is the only treated possibility. Further possibilities would be the inertial confinement and the confinement by gravitation.

[2] The reactivity is the averaged value of σv over a Maxwellian distribution of velocities v. Thereby $n_T \sigma v$ is the probability of a fusion reaction per time, for a T ion in the density n_T and velocity v and a reaction cross section σ [2].

with the temperature of electrons and ions, T_e and T_i, in units of energy, the losses by convection and heat conductivity combined in P_L and the radiation losses R [2].

In a stationary condition, these losses are compensated by the heating power P_{heat}. To combine the stationary state with the requirement $P_{heat} < P_{fus}$ the recirculation parameter η is introduced as $P_{heat} = \eta P_{fus}$ to parameterize the inequality. Therefore η takes values of $\eta = [\eta_{ignited}, 1]$, with $\eta_{ignited}$ explained below. Using eqs. (1.2) and (1.3) gives

$$P_{heat} = P_L + R = \frac{3nT}{\tau_E} = \eta P_{fus} \Rightarrow \frac{12T}{\eta Q_{fus} \langle \sigma v \rangle} = n\tau_E \tag{1.4}$$

where it is assumed that $T_e = T_i = T$. The right side of the arrow is known as the Lawson criterion. The expression $12T/\eta Q_{fus}\langle \sigma v \rangle$ is solely a function of the temperature T. Therefore eq. (1.4) can be plotted in a so-called Lawson diagram. This is shown in figure 1.1 for different values of η. A critical curve in this plot is $\eta = \eta_{ignited} = 0.2$, because the charged α-particles, as a product of the fusion reaction in eq. (1.1), carry approximately 20% of the energy. These α-particles are charged and therefore confined in the plasma. The neutrons are unaffected by the magnetic field and impinge in the wall, where they heat up a coolant for a steam generator. Thus, the total heating power of the plasma $P_{heat} = P_\alpha + P_{aux}$ is a combination of the heating power by the α-particles and external auxiliary heating systems. If the energy of the fusion born α-particles is sufficient to deliver the heating power in eq. (1.4) and no external heating power P_{aux} is required, the plasma is said to be ignited. DEMO is currently expected to work close to the ignited condition in the range of $\eta_{DEMO} = [0.225, 0.265]$ and thus, the plasma fulfills the Lawson criterion.

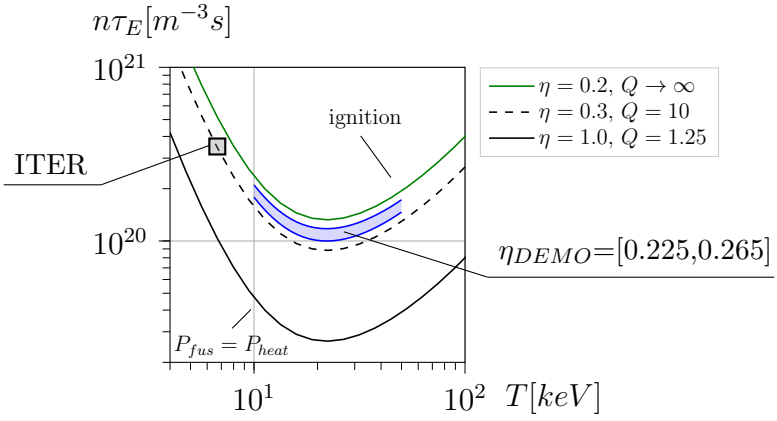

Figure 1.1: Lawson diagram with curves from eq. (1.4) for different η-values. The curves show, that there is a minimum in the temperature for fulfilling the Lawson criterion. The values of η are supplemented by values for the Q-factor, which is defined as $Q = P_{fus}/P_{aux}$, with the external auxiliary heating power P_{aux}. Hence, $Q = (\eta - 0.2)^{-1}$. The approximation for the operating range of DEMO is based on the engineering parameters of DEMO baseline 2018 in section 4.1.1 ($P_{fus} = 2\,\mathrm{GW}$, $P_\alpha = 0.2 P_{fus}$ and $P_{aux} = 50\,\mathrm{MW}...130\,\mathrm{MW}$) and the assumption, that DEMO operates in the region of the minimum temperature for the Lawson criterion. For comparison an estimation of the operating point of ITER is included, according to data from [2] for the inductive operation scenario. The plot is created based on eqs. from [2].

DEMO as an European project, for the utilization of nuclear energy in fusion power plants, is led by the organization EUROfusion. They published a road map, in which they outline the basic approach and milestones, about the realization of the project. This road map is depicted in figure 1.2. It is intended, to include all available information that is gained through experiments like ITER and other projects in material research. In the second time arrow from the bottom, one can see that it is not yet decided, whether the fusion power plant is going to be a tokamak or a stellarator. These are the two dominant types of reactors for magnetic confinement of a fusion plasma. This thesis works on the milestone of a consistent concept and focuses exclusively on the tokamak-version for DEMO. Therefore, the basic structure of a tokamak is introduced below.

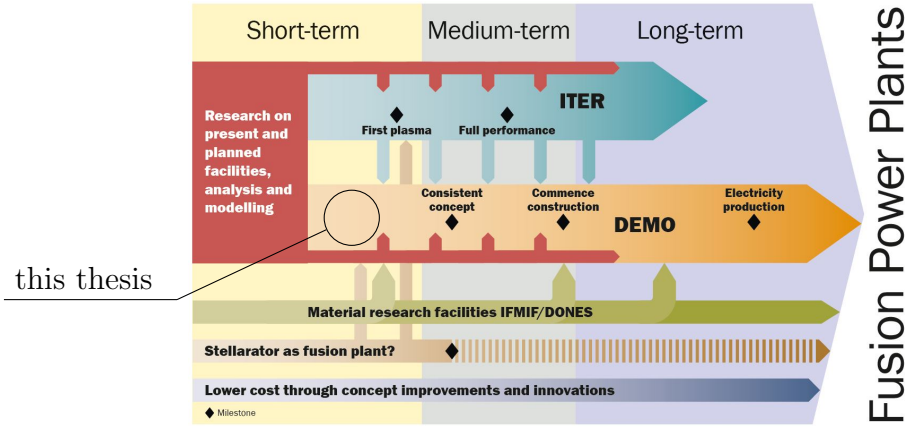

Figure 1.2: Road map with milestones of the European project DEMO, lead by EUROfusion. It is planned to include scientific insides from the predecessor ITER, which is designed as an experimental reactor,. Furthermore, material research and cost optimization programs contribute to DEMO. The decision, of whether the fusion power plant is going to be tokamak or a stellarator, needs to be decided at the milestone of the consistent concept, which is not reached while this thesis is written. Illustration from [3].

In a tokamak the plasma is confined by a coil system in a torus-shaped volume, which is enclosed by a vacuum vessel. The main parts of the coil system of a tokamak consist of poloidal field coils (PF coils), toroidal field coils (TF coils) and the central solenoid (CS). These coils are depicted in figure 1.3, together with an introduction of the poloidal and toroidal direction and a toroidal coordinate system $\{R, Z, \phi\}$. The fields generated by these coils are referred to as the vacuum induction fields. The toroidal field coils produce a magnetic induction field along the toroidal direction with the dependence $B_\phi \propto 1/R$, characteristic for toroidal coils. The magnetic field of the poloidal field coils is called the vertical field and is spanned by the vector components B_R and B_Z, whereas $B_\phi = 0$. A further magnetic field, the poloidal field, is generated by a plasma current flowing in the toroidal direction of the torus. This poloidal magnetic field is represented by the same vector components as the vertical field[3]. The plasma current is induced by a time dependent current in the central solenoid.

In a superposition of the poloidal magnetic field, generated by the plasma current, and the vertical field, generated from the poloidal field coils, the plasma can reach an equilibrium.

[3]Thereby a small contribution to the toroidal field due to the helically flowing plasma current is neglected.

However, this equilibrium is unstable against perturbations. A second option would be the confinement in a purely toroidal field, generated by the toroidal field coils. This confinement would be more stable against perturbations, but due to the $1/R$-dependence no equilibrium exists. The applied solution is to superpose all three magnetic fields and design them, to reach a stable equilibrium. Therefore the magnetic field lines twist around the minor axis of the torus helically, while they circulate around the major axis [4].

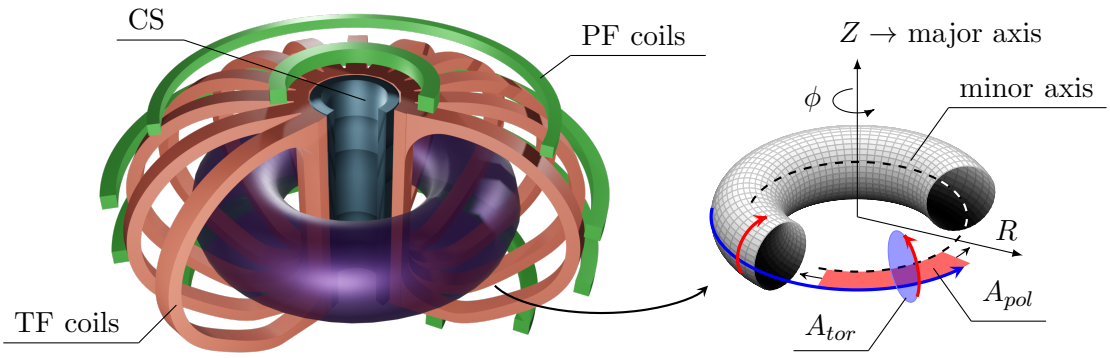

Figure 1.3: Illustration of the basic setup of a tokamak. The coil system of toroidal field coils (TF coils), poloidal field coils (PF coils) and central solenoid (CS) generates a magnetic field to confine the plasma. Therefore, the plasma levitates in the vacuum vessel, which encloses it inside the TF coils (see figure 4.3). An intuitive coordinate system for a tours is spanned by the coordinates $\{R, Z, \phi\}$, with radius R, height Z and toroidal angle ϕ, as depicted in the fundamental tours. The Z-axis in this system is called the major axis. Two basic directions are the toroidal direction, indicated by the blue arrow around the major axis, and the poloidal direction, indicated by the red arrows around the minor axis of the torus. These directions are used to reference a toroidal cross section A_{tor} enclosed by a poloidally circulating curve around the minor axis (blue plane), and a poloidal cross section A_{pol} enclosed by the minor axis and a toroidally circulating curve on the torus surface (red plane).

1.2 Motivation. Perturbation of axisymmetry by the toroidal field ripple

A tokamak plasma is in theory axisymmetric around the major axis of the torus. However, as it can be seen in figure 1.3, the axisymmetry is broken by the toroidal field coils. This can be seen more clearly in the schematic illustration in figure 1.4. The field lines of the toroidal induction field, generated by the toroidal field coils, are compressed underneath the coils and relieved in between them. This creates a spatial variation on the toroidal component of the magnetic field with a periodicity of the number of toroidal field coils, which is 16 for DEMO. This variation is the so-called toroidal field ripple. The toroidal field ripple is a 3D perturbation of the vacuum induction field and has an effect on the plasma confined in it. The plasma becomes corrugated, according to the variation in the toroidal field. There are two major reason, why 3D perturbations of a plasma are investigated.

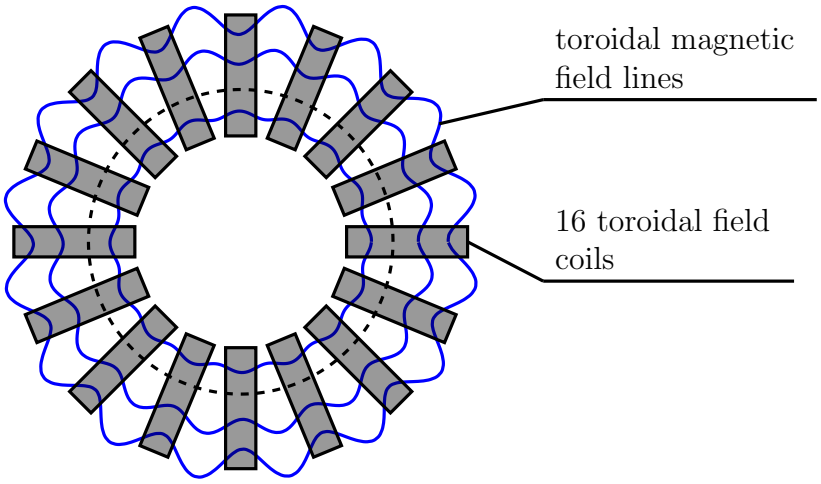

Figure 1.4: Schematic illustration of the toroidal field ripple in top view from the coil system shown in figure 1.3, with a strongly enlarged amplitude for illustration purposes. From the coil system only the toroidal field coils are depicted, because the toroidal field ripple is an unintentional result of the finite number of toroidal field coils. As planned for DEMO, 16 toroidal field coils are depicted. The blue lines represent the toroidal magnetic field and show the radial widening in the space between the coils. The bigger the space between the coils is, the larger is the widening. Therefore the ripple is expected to be highest at the outboard side. This side is also called the low-field side, because of the $1/R$-dependence. Correspondingly, the inboard side is called the high-field side.

First, the fast ions in the plasma are important for the plasma heating and the energy confinement. They are either orbiting around the major axis of the torus (passing particles) or moving back and forth in a magnetic mirror, formed by high-field and low-field side of the magnetic field (trapped particles). In an axisymmetric plasma both are confined, but trapped particles can leave the plasma if it is corrugated in the toroidal direction [5]. These losses are called ripple losses and need to be minimized for an improved energy confinement, as well as to guarantee allowable heat loads on the first wall [6].

Second, in the physical model of the so-called ideal MHD (**M**agneto**H**ydro**D**ynamic), the plasma is described by nested, toroidal flux surfaces. These flux surfaces are onion-like layers, where each layer has a constant kinetic pressure. Therefore, a pressure gradient can be established with high pressure in the core of the plasma and no pressure at the plasma edge, for compatibility to the surrounding structure. Due to the break of the axisymmetry by 3D perturbations the structure of nested flux surfaces can be interrupted. Such regions have substantial radial transport of energy and thus, reduce the energy confinement time τ_E, as described in more detail in section 2.3. Although it is explained in section 2.3, that the toroidal field ripple is not expected to interrupt the structure of nested flux surfaces, the 3D modelling of the coil systems, as it is needed for the study of the toroidal field ripple, is important for investigation of further 3D perturbations.

As part of the investigations of 3D perturbations, this thesis has the aim to compute 3D flux surfaces in the ideal MHD equilibrium. Thereby the focus is on the influence of the toroidal field ripple on the flux surfaces geometry. The here presented investigation is addressed by

means of two main objectives:

1. Coupling of a code system for the computation of flux surfaces in 3D vacuum induction fields in the physical picture of the static ideal MHD equilibrium, starting with profiles from turbulent transport simulations.
2. Compute the plasma response to the toroidal field ripple for the latest DEMO baselines of EUROfusion, by using the new code system.

1.3 Structure and outline of this thesis

In the conceptual phase of DEMO, the toroidal field ripple in the vacuum induction field was minimized by designing the geometry of the ferromagnetic inserts[4]. However, the computations carried out until now did not include the plasma response. This thesis continues these computations, with the 3D modelling of the MHD equilibria of a DEMO tokamak. Thus, the plasma response to the toroidal field ripple can be investigated. For the computations of this work, a code system is developed, with the 3D MHD equilibrium solver PARVMEC as central building block of the newly coupled code system. Three achievements of this code system are:

- the coupling of the versatile transport simulation code ASTRA to the 3D free boundary solver PARVMEC for the computation of 3D ideal MHD equilibria,
- the creation of a parametric input generator to translate 3D coil systems into MAKEGRID format for the computation of vacuum induction fields
- and the inclusion of ferromagnetic inserts, inside the vacuum vessel, in a coil model, for the computation of their effect on the 3D vacuum induction field with MAKEGRID.

The developed code system is applied successfully for the computation of the plasma response to the toroidal field ripple in two plasma scenarios. Both confirm the expected non-resonant plasma response, shown in this thesis by comparison of the toroidal field ripple in the vacuum induction field and the corrugation of the plasma on the **L**ast **C**losed **F**lux **S**urface (LCFS), as computed by PARVMEC. Furthermore, it is shown for the L-mode, that 3D free-boundary simulations differ up to 26% in the amplitude of the flux surface corrugation, relative to the vacuum approximation. This indicates the need for inherent 3D simulations.

The rest of this thesis is structured as follows. In chapters 2 and 3 the basic physical considerations and employed numerical tools relevant to this thesis are introduced. Chapter 2 focuses on the physical background and chapter 3 on the algorithmic aspects of existing codes used in the code system. Next, the baseline of the here presented work is described in chapter 4. The baseline consists of the plasma scenarios supplied from ASTRA transport simulations and the geometry of the coil system. Chapter 5 explains in detail the coupling of the code system. Thereby the newly developed codes PIGEN (**P**ARVMEC **I**nput **GEN**erator) and MIGEN (**M**AKEGRID **I**nput **GEN**erator) are presented. Chapter 6 describes the result of the plasma response to the toroidal field ripple of L-mode and H-mode and the effect of ferromagnetic inserts, as computed by the developed code system. Finally, a conclusion and outlook are given in chapter 7.

[4]Ferromagnetic inserts are volumes, inside the vacuum vessel wall, filled with ferromagnetic material, for the reduction of the toroidal field ripple. They are described in detail in section 5.3.3.

2 Relevant physical background

2.1 Equilibrium in the ideal MHD picture

In this thesis the 3D flux surfaces are computed in a physical model called the static ideal MHD model. The ideal MHD model is a fluid model, which is applied for the description of fusion plasmas. Although it is a physical model resulting from a cascade of simplifications, it is able to describe the equilibrium [4]. In the following this cascade is outlined, to enable a classification of the contained physics in the results of this thesis. This outline is based on [4], where all equations in this section can be found with further details.

First of all, a fully ionized plasma of a tokamak consists of electrons and ions of different species. The starting point for capturing the physics is a statistical description of each species, by the distribution function $f_\alpha(\vec{r}, \vec{v}, t)$ of species α for the position $\vec{r}$ and the velocity $\vec{v}$ at a given time t. The time evolution of this distribution function is given through a coupling of the Boltzmann-equation

$$\frac{\partial f_\alpha}{\partial t} + \vec{v} \cdot \vec{\nabla}_r f_\alpha + \frac{1}{m_\alpha} Z_\alpha e(\vec{E} + \vec{v} \times \vec{B}) \cdot \vec{\nabla}_v f_\alpha = \left(\frac{\partial f_\alpha}{\partial t}\right)_c \tag{2.1}$$

to the Maxwell-equations

$$\vec{\nabla} \times \vec{E} = -\frac{\partial \vec{B}}{\partial t} \tag{2.2a}$$

$$\vec{\nabla} \times \vec{B} = \mu_0 \vec{j} + \frac{1}{c^2} \frac{\partial \vec{E}}{\partial t} \tag{2.2b}$$

$$\vec{\nabla} \cdot \vec{E} = \frac{\sigma}{\epsilon_0} \tag{2.2c}$$

$$\vec{\nabla} \cdot \vec{B} = 0 \tag{2.2d}$$

because the force term in the Boltzmann-eq. is given by the general Lorentz-force[1]. Eq. (2.1) contains the elementary charge e, the atomic mass of the species m_α and its atomic number Z_α. The current density $\vec{j}$ and the charge density σ in the Maxwell-eqs. (2.2) are related to the distribution function by

$$\vec{j} = \sum_\alpha Z_\alpha e \int \vec{v} f_\alpha d^3v \tag{2.3a}$$

$$\sigma = \sum_\alpha Z_\alpha e \int f_\alpha d^3v \tag{2.3b}$$

Based on this set of coupled eqs., the following steps lead to the ideal MHD picture.

[1] A derivation of the general Boltzmann-eq. can be found in [7].

1. *Forming moments of eq.* (2.1) *for the two-fluid picture.*

   $\rightarrow f_\alpha(\vec{r},\vec{v},t) \Rightarrow \{n_\alpha, \vec{u}_\alpha, p_\alpha\}(\vec{r},t)$

   This is done by multiplying first the eq. (2.1) with powers of the velocity and then integrating over the velocity space. For the derivation of the ideal MHD picture the moments related to mass, momentum and energy are used (exponents 0,1,2). By this integration the distribution function is translated into the so called two-fluid picture of a hydrogenic plasma ($Z_i = -Z_e = 1$), consisting of eqs. for the densities n_α, the fluid velocities $\vec{u}_\alpha$ and the pressures p_α. However, this set of eqs. is not closed. The closure is achieved below, by approximation of the higher moments in the integrals based on the assumption of collision dominated distribution functions.

2. *Quasi-stationary approximation of Maxwell-eqs.*

   $\rightarrow \vec{\nabla} \times \vec{B} = \mu_0 \vec{j} + \frac{1}{c^2}\frac{\partial \vec{E}}{\partial t} \Rightarrow \vec{\nabla} \times \vec{B} \approx \mu_0 \vec{j}$

   The displacement current $\partial\vec{E}/\partial t$ is neglected in this approximation. This limits the phase velocity of electromagnetic waves, as well as the thermal velocities of electrons and ions, to be small compared to the speed of light c.

3. *Quasi-neutral approximation of the plasma.*

   $\rightarrow n_i \approx n_e = n$

   This approximation leads to again eliminating high frequencies and short wave lengths in the contained phenomena. For $n_i \approx n_e$ to be a valid approximation, the considered processes need to take place with frequencies below the plasma frequency, so that electrons can eliminate local imbalances and the length scales need to be big, compared to the Debye length[2].

4. *Neglecting electron mass m_e with respect to ion mass m_i for the single fluid picture.*

   $\rightarrow \{n, \vec{u}_i, \vec{u}_e, p_i, p_e, T_i, T_e\} \Rightarrow \{\rho, \vec{v}, \vec{j}, p, T\}$

   The transition of a two-fluid picture of ions and electrons to a single-fluid picture is accomplished by introducing the density $\rho = m_i n$, the velocity $\vec{v} = \vec{u}_i$, the current density $\vec{j} = en(\vec{u}_i - \vec{u}_e)$ and the pressure $p = p_i + p_e = 2nT$ with the temperature $T = T_i = T_e$ of a single fluid.

5. *For the ideal MHD limit, electron and ion distributions are assumed to be collision dominated.*

   The assumption of collision dominated electrons and ions leads to Maxwellian distribution functions, for which the pressure tensor is isotropic. This pressure tensor is contained in the eqs. besides the scalar pressure p, until the ideal MHD limit is applied. By this assumption higher moments of eq. (2.1) can be approximated and subsequently be neglected for the ideal MHD picture. Thereby the plasma is considered as perfect conductor, giving rise to the name 'ideal' MHD.

[2]The Debye length in plasma physics is the characteristic length for the shielding of the Coulomb potential [8].

The resulting eqs. for the ideal (single fluid) MHD picture are

$$\frac{\partial \rho}{\partial t} + \vec{\nabla} \cdot (\rho \vec{v}) = 0 \tag{2.4a}$$
$$\rho \frac{d\vec{v}}{dt} = \vec{j} \times \vec{B} - \vec{\nabla} p \tag{2.4b}$$
$$\frac{d}{dt}\left(\frac{p}{\rho^\gamma}\right) = 0 \tag{2.4c}$$
$$\vec{E} + \vec{v} \times \vec{B} = 0 \tag{2.4d}$$
$$\vec{\nabla} \times \vec{E} = -\frac{\partial \vec{B}}{\partial t} \tag{2.4e}$$
$$\vec{\nabla} \times \vec{B} = \mu_0 \vec{j} \tag{2.4f}$$
$$\vec{\nabla} \cdot \vec{B} = 0 \tag{2.4g}$$

with the convective derivative $\frac{d}{dt} = \frac{\partial}{\partial t} + \vec{v} \cdot \vec{\nabla}$ and the adiabatic coefficient γ.

As mentioned in the beginning of this section, the computations of the 3D flux surfaces in this thesis are performed in the static ideal MHD picture. This model is received from eqs. (2.4) by neglecting flow $\vec{v} = 0$ and time dependent contributions. As result the basic 3D equilibrium eqs.

$$\vec{j} \times \vec{B} = \vec{\nabla} p \tag{2.5a}$$
$$\vec{\nabla} \times \vec{B} = \mu_0 \vec{j} \tag{2.5b}$$
$$\vec{\nabla} \cdot \vec{B} = 0 \tag{2.5c}$$

are obtained.

2.2 Flux surfaces and magnetic flux coordinates

A property of the static 3D equilibrium, described by eqs. (2.5), is, that the magnetic field $\vec{B}$ and the current density $\vec{j}$ are on surfaces with constant pressure p. This can be readily seen by forming the dot product of eq. (2.5a) with either of the vectors, leading to $\vec{B} \cdot \vec{\nabla} p = 0$ and $\vec{j} \cdot \vec{\nabla} p = 0$. These surfaces are called flux surfaces. The only mathematical solution for these flux surfaces in 3D space are toroidal surfaces [9], from what follows that the structure of the equilibrium is described by toroidal, nested flux surfaces. Approximately at the minor axis of the tours (figure 1.3) these nested toroidal surfaces shrink to a single curve without volume. This curve is called the magnetic axis. Besides the toroidal coordinate system $\{R, Z, \phi\}$, which is intuitively introduced in the introduction, some of the explanations in this work make use of a coordinate system, which is known as magnetic coordinate system. This coordinate system

is a local curvilinear coordinate system, based on coordinates related to flux surfaces. The three coordinates are denoted by $\{\rho, \theta, \zeta\}$.

The first coordinate in the magnetic flux coordinates, ρ, is chosen be a label for the flux surfaces. This means, that a flux surface needs to be uniquely identified by a value for ρ. Potential choice for ρ is the confining pressure $\rho = p$. However, each quantity identifying a flux surface can be used. As introduced in subsequent chapters, ρ will be identified by functions of the toroidal flux Φ in this work. Φ is the magnetic flux through a toroidal cross section A_{tor}, introduced in figure 1.3, therefore $\Phi = \int_{A_{tor}} \vec{B} \cdot d\vec{A}$. Analogous the poloidal flux χ is defined by $\chi = \int_{A_{pol}} \vec{B} \cdot d\vec{A}$ and could be used as radial coordinate. The second coordinate, θ, is an angle-like coordinate for the poloidal direction. The values of θ are $[0, 2\pi]$ for one revolution around the minor axis of the torus. Analogous is the angle-like coordinate ζ for the toroidal direction defined. A revolution around the major axis of the tours spans ζ-values of $[0, 2\pi]$. They are called angle-like, because they do not necessarily coincide with geometrical angles around the major and minor axes. Each transformation

$$\tilde{\theta} = \theta + f(\rho, \theta, \zeta) \tag{2.6}$$

$$\tilde{\zeta} = \zeta + g(\rho, \theta, \zeta) \tag{2.7}$$

with 2π-periodic function f and g give equally valid coordinates. A ζ-coordinate curve for $\rho = const.$, $\theta = const.$ is located on a flux surface and same is valid for θ-coordinate curve. Therefore their covariant bases vectors

$$\vec{e}_\theta = \frac{\partial \vec{r}}{\partial \theta} = \sqrt{g}(\vec{\nabla}\zeta \times \vec{\nabla}\rho) \tag{2.8}$$

$$\vec{e}_\zeta = \frac{\partial \vec{r}}{\partial \zeta} = \sqrt{g}(\vec{\nabla}\rho \times \vec{\nabla}\theta) \tag{2.9}$$

lie in a flux surface. They are related to the contravariant basis vector $\vec{e}^\rho = \vec{\nabla}\rho$ by

$$\vec{\nabla}\rho = \sqrt{g}(\vec{e}_\theta \times \vec{e}_\zeta) \tag{2.10}$$

with the Jacobian $\sqrt{g} = [\vec{\nabla}\rho \cdot (\vec{\nabla}\theta \times \vec{\nabla}\zeta)]^{-1}$ [10].

Another flux surface quantity, which is relevant for this work (but not used as coordinate), is the safety factor q. It is closely related to the average rotational transform angle

$$\bar{\iota} = \frac{1}{2\pi} \lim_{n\to\infty} \frac{\sum_{k=1}^{n} \iota_k}{n} \tag{2.11}$$

normalized to 2π, where ι_k is the difference $\Delta\theta$ in the position of a field line after the k-th toroidal circulation ($\Delta\zeta = 2\pi$). The q-profile $q = q(\rho)$ is given by [10]

$$q(\rho) = \frac{1}{\bar{\iota}(\rho)} \tag{2.12}$$

2.3 3D perturbations

After the introduction of flux surfaces in the ideal MHD equilibrium and magnetic flux coordinates, this section picks up the motivation of this thesis to discuss the two major objectives in more detail. The first objective is the development of a code system for the computation of flux surfaces under the influence of 3D perturbations in the ideal MHD equilibrium, starting with profiles from turbulent transport simulations. 3D perturbations in general are non-axisymmetric magnetic perturbations and must be considered when designing a fusion power plant. The reason for this can be seen by considering flux surfaces. In tokamaks with axisymmetry, the structure of nested flux surfaces is rigorously present, but without axisymmetry some flux surfaces can expand to finite volume, as described below [10].

There are two types of flux surfaces: Rational and irrational flux surfaces. Irrational flux surfaces are made of non-closing magnetic field lines and cover ergodically the whole surface. Rational flux surfaces close themselves after a number of toroidal revolutions. Rational flux surfaces show the ability to open so-called magnetic islands, if a perturbation aligns with the magnetic field of the flux surface. In this case error fields, perpendicular to the flux surfaces, are induced, which alternate sign around the poloidal circumference. These error fields detach the magnetic field lines from the flux surface and twist them, additionally to the twist around the magnetic axis in the center, around a new axis of the magnetic island [8].

Perturbations with such an alignment are called resonant magnetic perturbations. They penetrate the magnetic surfaces and can cause the magnetic field lines to fill stochastic volumes, as shown in figure 2.1. Flux surfaces are surfaces with constant pressure p (see section 2.1). If now flux surfaces are radially extended to volumes, these volumes do not contain a pressure gradient. Hence, these stochastic volumes allow enhanced radial transport out of the plasma [4]. Furthermore, particles on nested flux surfaces around magnetic island are transported parallel to magnetic field lines to regions more outside the plasma, as indicated in figure 2.1. Particles leaving magnetic surfaces at this position of the island due to collisions are another contribution to enhanced radial transport.

The second major objective of the motivation in section 1.2 is the computation of the plasma response to the toroidal field ripple, as a 3D perturbation of the magnetic vacuum induction field. Due to the finite number of toroidal field coils, the strength of the vacuum induction field generated by them is denser inside a toroidal field coil and attenuated in between the coils. Because of the regular placement of the coils, in the toroidal direction, a periodic ripple in the toroidal field arises. For the investigations of the plasma response a measure for the extent of the toroidal vacuum field ripple $\tilde{\delta}(R, Z)$ is introduced by

$$\tilde{\delta}(R, Z) = \frac{\max_\phi[B_{\phi,vac}(R, Z, \phi)] - \min_\phi[B_{\phi,vac}(R, Z, \phi)]}{\max_\phi[B_{\phi,vac}(R, Z, \phi)] + \min_\phi[B_{\phi,vac}(R, Z, \phi)]} \tag{2.13}$$

with $\max_\phi$ and $\min_\phi$ over of the toroidal angle ϕ at a $\{R, Z\}$ point. This measure is based on the toroidal component of a magnetic vacuum induction field $B_{\phi,vac}$, generated by the toroidal field coils. This definition of $\tilde{\delta}(R, Z)$ is adopted from [11], because results of following chapters are compared to [11].

Through the action of forces from the magnetic field to the plasma and the influence of the plasma back to the magnetic field, a coupling of perturbations to the flux surfaces can occur.

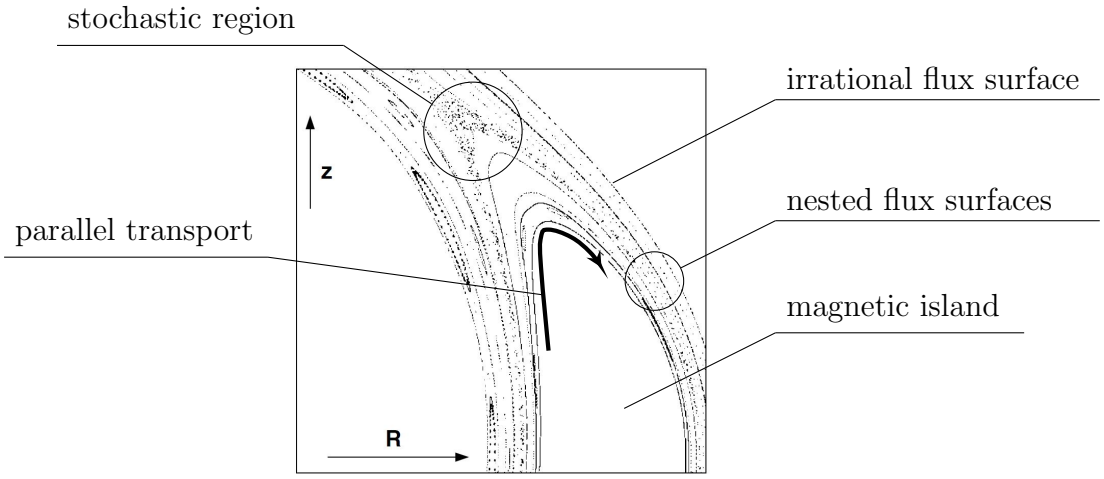

Figure 2.1: Poincare plot of a poloidal cross section for a non-axisymmetric plasma with magnetic islands. Each point in the plot is a puncture of a traced magnetic field line during the circulation around the major axis of the torus. Above the magnetic island the field lines are detached from magnetic surfaces and form a stochastic region. Furthermore, nested flux surfaces around a magnetic island allow particle transport parallel to the magnetic field lines, what cause additional radial transport. Figure from [8], supplemented with labels.

This coupling is described by the so-called plasma response. To investigate the influence of the toroidal field ripple on the plasma, the plasma response is measured in this thesis by the amplitude of the corrugation of flux surfaces $\delta(R, Z)$. The amplitude $\delta(R, Z)$ is defined by

$$\delta(R, Z) = \max_\phi[\xi(R, Z, \phi)] - \min_\phi[\xi(R, Z, \phi)] \tag{2.14}$$

with the absolute value ξ of the corrugation vector $\vec{\xi}$, which is explained in figure 2.2 and again $\max_\phi$ and $\min_\phi$ over the toroidal angle ϕ at a $\{R, Z\}$ point. $\xi(R, Z, \phi)$ is positive if the flux surfaces are displaced radially outwards and negative, if the displacement is directed inwards. For the computation of $\delta(R, Z)$ the algorithm developed in [12] is used in this work.

An estimation, if a 3D perturbation is expected to couple resonant or non-resonant to a flux surface, can be given by decompose the perturbation into poloidal and toroidal Fourier harmonics, m_{per} and n_{per}. If the ratio m_{per}/n_{per} takes values of the q-profile, it can cause resonant perturbations. This can be seen by introducing an analogous quantity to the rotational transform $\bar{\iota}_{per}$ for the perturbation as

$$\bar{\iota}_{per} = \frac{\lambda_{pol}}{\lambda_{tor}} \Rightarrow q_{per} = \frac{m_{per}}{n_{per}} \tag{2.15}$$

with the poloidal and toroidal wavelength λ_{pol} and λ_{tor} of the perturbation. For the toroidal field ripple $n_{per} = 16$ is expected in combination with a low number of poloidal harmonics m_{per}, because of the D-shaped cross section of the toroidal field coils, so $q_{per} < 1$. In chapter 4 q-profiles of two plasma scenarios used this work are depicted, both with $q(\rho) > 1$. Therefore, the toroidal field ripple of the toroidal field coils is not expected to be a resonant perturbation.

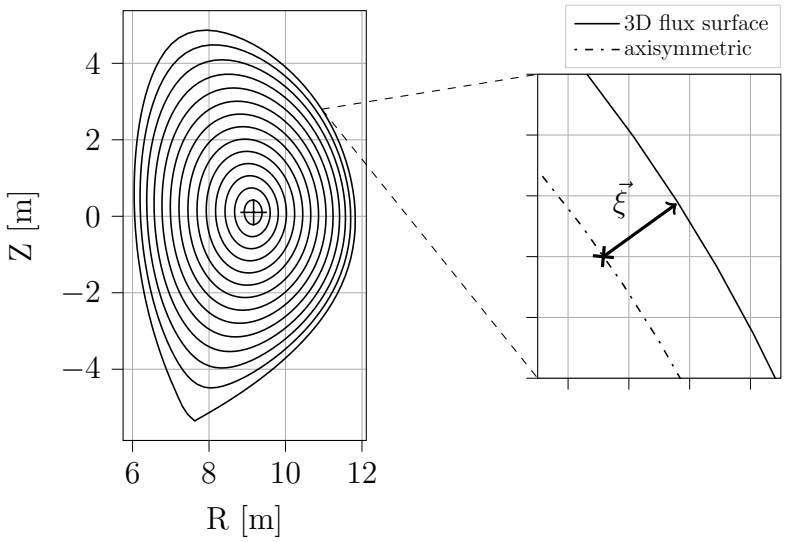

Figure 2.2: On the left side an example of nested flux surfaces in a poloidal cross section is shown. On the right side a zoomed detail is depicted, to visualize the corrugation vector $\vec{\xi}$ for a single point on a flux surface. For the definition of $\vec{\xi}$ the 2D axisymmetric and the 3D solutions of a flux surface are required. The vector is always perpendicular to the axisymmetric flux surface at the considered point and points radially outwards to the coordinate of the 3D solution of the same flux surface, which can be displaced relative to the axisymmetric solution, depending on the toroidal position ϕ. The absolute value of the corrugation vector is negative, if the 3D flux surfaces are displaced inwards. $\vec{\xi}$ is computed for several points on a 3D grid.

2.4 L-mode and H-mode

A plasma scenario is a set of quantities and profiles, defining the state of the plasma. There are several known plasma scenarios, with different characteristics. However, for this thesis two of them are relevant, the L-mode (low-confinement mode) and H-mode (high-confinement mode). Both are introduced in this section.

The L-mode can be viewed as starting point for reaching further plasma states. By heating the D-T mixture it becomes ionized and is confined by the coil system. The kinetic profiles of this mode fulfill the necessity, that pressure and temperatures are low at the plasma boundary and increase towards the magnetic axis. In figure 2.3 the profiles for electron and ion densities, $n_e(\rho)$ and $n_i(\rho)$, together with the electron and ion temperatures, $T_e(\rho)$ and $T_i(\rho)$, are shown for an L-mode. An example for the pressure profile of an L-mode can be seen in section 4.1.1.

The second relevant mode for this thesis is the H-mode. This plasma state is reached from the L-mode by the so-called L-H transition. This transition is achieved by exceeding a certain threshold of heating power P_{LH}, which can be determined by the scaling law

$$P_{LH,scale} = 0.049 \cdot \bar{n}_e^{0.72} \cdot B_0^{0.8} \cdot S^{0.94} \tag{2.16}$$

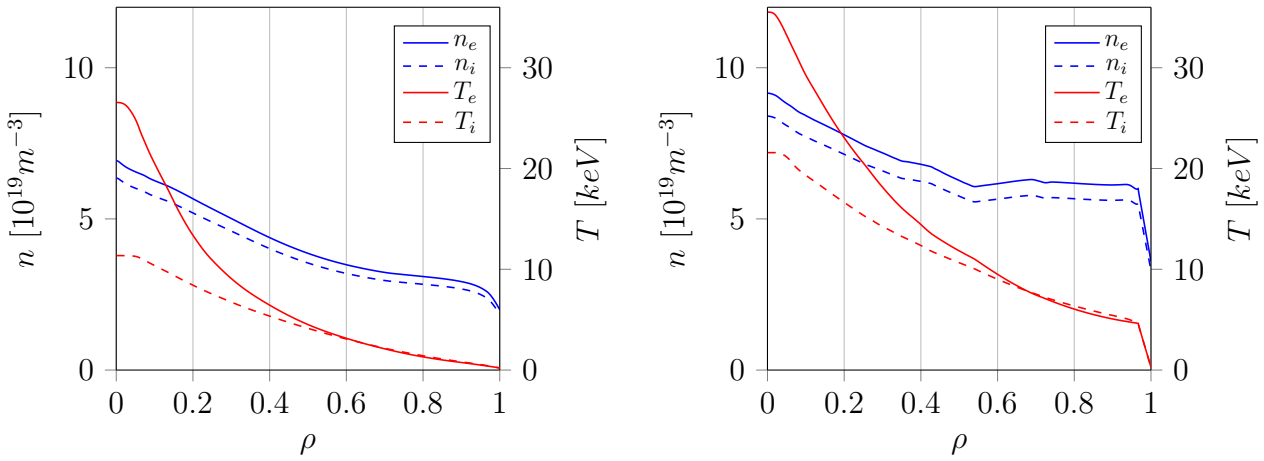

(a) L-mode

(b) H-mode

Figure 2.3: Density and temperature profiles, $n(\rho)$ and $T(\rho)$, for electrons and ions as function of the used flux surface label $\rho = \sqrt{\Phi/\Phi_{edge}}$ (Φ: toroidal magnetic flux). $\rho = 0$ is the magnetic axis and $\rho = 1$ the plasma boundary. The plotted data corresponds to the L-mode and H-mode, which are investigated in this thesis, as described in section 4.1.

with the line averaged[3] electron density $\bar{n}_e$ in $10^{20}m^{-3}$, the toroidal magnetic field on the minor axis B_0 in T and plasma surface area S in m^2. $P_{LH,scale}$ is then given in MW [13][4].

A characteristic feature of the H-mode is depicted in figure 2.3. In comparison to the L-mode the gradients of the densities and the temperatures show a steep increase near the plasma boundary. These steep gradients translate to the pressure profile, as described in section 4.1.2. They are a result of a so-called **E**dge-**T**ransport-**B**arrier (ETB). This ETB is a layer of flux surfaces near the plasma edge, suppressing turbulent transport. The ETB is a result of a $\vec{E} \times \vec{B}$ shear flow induced by a radial electric field E_r, where $\vec{E} \times \vec{B}$ shear flow is a drift movement of the particles in a direction perpendicular to the electric and magnetic field. The electric field is a radial electric field E_r, induced by a ion temperature gradient $\vec{\nabla}T_i$ in the plasma edge [13].

The suppression of turbulent transport improves the energy confinement and therefore increases τ_E. Thus, H-modes are one of the most promising candidates for electricity production in fusion power plants [14, 15].

Although the H-mode and the L-H transition are experimentally well investigated and measured, the physical modelling for calculations and simulations are an active area of research. A current issue of this research, is the transfer of energy into so-called zonal flows as a potential trigger for the L-H transition. In combination with a sufficient large ion temperature gradient $\vec{\nabla}T_i$, driving a ion heat flux across the plasma boundary, the radial electric field E_r could be generated [13].

[3]The so-called line average is the average over the radial coordinate, here ρ.

[4]This scaling law is only valid for the high electron density branch. In general the dependence of P_{LH} is non-monotonic in the electron density [13].

3 Description of existing numerical tools

3.1 ASTRA

3.1.1 Building transport simulations using TGLF

ASTRA is a build system for the creation of code to solve transport problems. It enables the flexible implementation of ongoing progress in understanding transport phenomena achieved in theory and experiments. The flexibility to adjust the code for a specific transport analysis is given by a modular setup. These modules are often coupled, because the same physical quantity appears in many modules. The approach of a build systems meets the requirement of maintainability of these coupled modules [16]. Figure 3.1 depicts the basic workflow of the creation of a transport simulation with ASTRA. In this and the following section the focus is on the relevant aspects of the underlying provision study [14] of this thesis. This provision study provides output files of ASTRA simulations, which are then further processed to investigate the plasma response to the toroidal field ripple, as described in section 5.

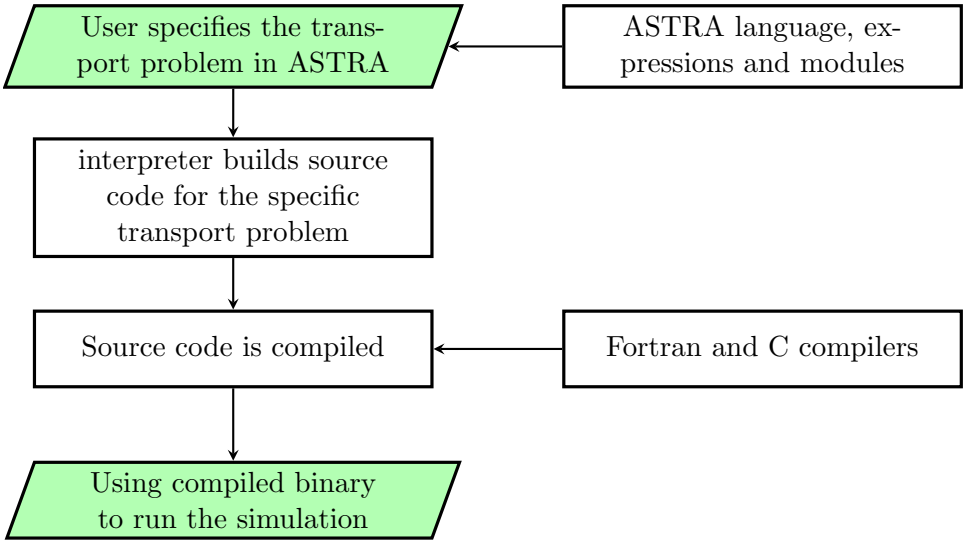

Figure 3.1: The ASTRA environment provides a language suitable for transport problems, expressions and modules for the user to specify the transport problem. A simulation can contain several blocks for different tasks, which are connected through the ASTRA environment. Chart is created following [16].

ASTRA simulations have in common, that they solve a system of 1D diffusion equations, which is presented in [16]. These are, for instance, electron and ion densities and temperatures[1], a 2D

[1]Other plasma species can be included.

axisymmetric equilibrium and other user defined modules, as explained in figure 3.1. The 2D equilibrium is used to close the diffusion equation system, even though the concrete solver is implemented as a module [16]. The relevant solver for this thesis is SPIDER, see section 3.1.2. In the above mentioned provision study the diffusion coefficients of the equation system solved in ASTRA contain neoclassical and turbulent transport contributions. The applied turbulent transport model is the trapped gyro-Landau-fluid (TGLF) model [17]. For the completeness of the existing codes a brief introduction to TGLF is presented. For the details of the underlying transport simulations of the thesis, the reader is referred to the provision study [14].

The intention of TGLF is the accurate description of linear drift wave[2] eigenmodes in a computationally efficient manner. Therefore a GLF equation system, which basically consists of gyroaveraged velocity and momentum equations, is used. These equations include passing and trapped particles [17]. Passing particles circulate around the magnetic axis along the field lines, while on the other hand trapped particles move in so called banana orbits, because they are reflected by a magnetic mirror passing from low field to high field side [8]. The inclusion of both types of particles allows the modelling of electron temperature gradient driven modes with low wave numbers. These are often the most unstable modes in the outer 1/3 of the plasma. The proper modelling of this region is crucial, for the transport prediction out of the plasma [17].

The TGLF equation set is made up of six moment equations of the linearized electrostatic gyrokinetic equation[3]. These six moments are the density, parallel velocity, parallel pressure, total pressure, parallel energy flux and total energy flux. The total velocity together with parallel velocity has the advantage of a simple scaling with the trapped particle fraction, if they are defined by the integration over the velocity space of the trapped particles. The system of the six moment equations is closed, by expressing higher velocity moments, occuring inside the moment equations, by the above mentioned lower order moments [17].

Computational extensive gyrokinetic simulations show, that turbulence contains a non-linear saturation behaviour. Thus, quasilinear weights are implemented in saturation models in the substantially faster TGLF code. The first saturation model SAT0 is improved by take mode coupling into account [18]. The resulting model SAT1 is extended by including geometric factors to account for Shafranov shift and elongation [19]. This version of TGLF is referred to as TGLF-SAT1geo and is the version which is applied in the underlying ASTRA simulations of this thesis, to compute the turbulent transport coefficients.

3.1.2 Equilibrium solver SPIDER

As explained in the previous section, ASTRA solves a set of 1D diffusion equations to compute kinetic profiles. This set of equations is under-determined and for the closure of the system a 2D axisymmetric equilibrium is solved simultaneously and self consistent with the diffusion system. Both, transport and the equilibrium quantities, do vary with the 'in-ASTRA'-time of the simulation [16]. The main components of the provision study [14] and the interplay between transport and equilibrium solver are shown in figure 3.2.

[2]Drift waves are pressure gradient driven waves with a phase velocity in comparable magnitude to the diamagnetic drift velocity [8].

[3]The moments are gained in a similar way to the moments of the kinetic equations used for the ideal MHD model in section 2.1. The derivation of them is described in [17].

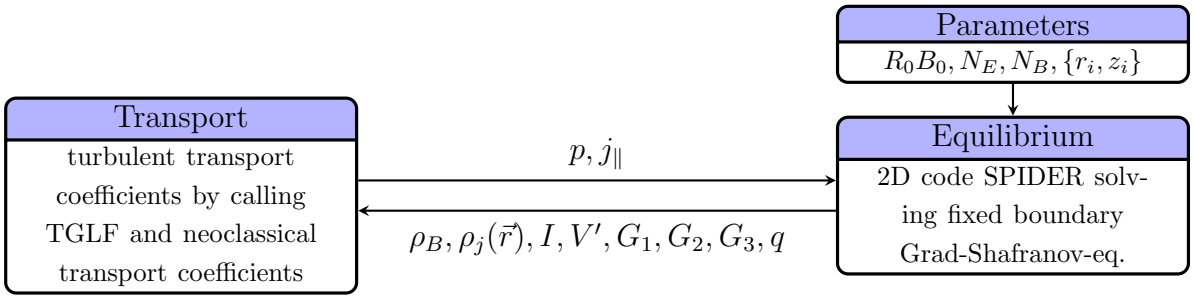

Input to the equilibrium module		**Output** from the equilibrium module	
R_0B_0	boundary value of I	ρ_B	boundary value of ρ
N_B	boundary-grid size	$\rho_j(\vec{r})$	shape of every flux surface
$\{r_i, z_i\}$	boundary shape	$I(\rho_j)$	poloidal current
N_E	ρ-grid size	$V'(\rho_j)$	volume derivative
ρ_j	ρ-grid	$G_1(\rho_j)$	} metric characteristics
$p(\rho_j)$	pressure profile	$G_2(\rho_j)$	
$j_\parallel(\rho_j)$	current density profile	$G_3(\rho_j)$	
		$q(\rho_j)$	q-profile

Figure 3.2: The transport module solves the diffusion and transport equations given in [16] in user defined time steps in the so called 'in-ASTRA'-time. The necessary transport coefficients for turbulent transport are obtained by calling TGLF code after a specified number of time steps and the neoclassical transport coefficients are given by formulas according to [14]. After another specified number of time steps the equilibrium module is called for the closure of the ASTRA transport model. This figure is created according to [16] and [14].

The above depicted coupling of TGLF transport system and equilibrium solver SPIDER was successfully used in [20] to reproduce a plasma discharge in ASDEX Upgrade and used again in the provision study [14] for this thesis. Thereby implemented equilibrium solver SPIDER can be operated in several modes. A overview of the capabilities of SPIDER is given in [21]. In the provision study [14] SPIDER is used as a fixed-boundary equilibrium solver with a static ρ-grid. In this mode SPIDER takes a prescribed plasma boundary and computes the inner flux surfaces as solution of the Grad-Shafranov-eq.[4]. To obtain a well-defined MHD problem, additional profiles need to be prescribed. In the provision study [14] the pressure profile and the q-profile are prescribed in the simulations and used in SPIDER when calling the equilibrium module, together with the computed current density profile and further parameters, as depicted in figure 3.2 for a general coupling of the equilibrium module.

[4]Eq.(2.5) can be transformed to the Grad-Shafranov-eq. by assuming axisymmetry, as shown in [4].

3.2 MAKEGRID

This code is used to compute static magnetic fields of a given set of coils in vacuum[5]. A coil is modelled by straight filaments in Cartesian coordinates, each representing an infinitely thin conductor. Complex coil geometries can be approximated by linking numerous filaments. Also spatially extended coils can be represented by several windings of line conductors next to each other. Thus the magnetic field of a coil $\vec{B}^{coil}$ is given by the fields of single conductor $\vec{B}^{cond}$ through

$$\vec{B}^{coil} = \sum_{i=1}^{m} \vec{B}_i^{cond} \tag{3.1a}$$

$$\vec{B}^{cond} = \sum_{j=1}^{L} \vec{B}_{i,j}^{fil} \tag{3.1b}$$

$$\vec{B}_{i,j}^{fil} = \frac{\mu_0}{4\pi} I_i^{cond} \int_0^l \frac{\hat{k}_j \times (\vec{r} - \vec{r}_j(l))}{|\vec{r} - \vec{r}_j(l)|^3} \, |\vec{r}_{j+1} - \vec{r}_j| \tag{3.1c}$$

with the field of a single straight filament $\vec{B}_{i,j}^{fil}$ by the Biot-Savart law.

$$\hat{k}_j = (\vec{r}_{j+1} - \vec{r}_j) / |\vec{r}_{j+1} - \vec{r}_j|$$

is the unit vector from one filament to the next. MAKEGRID outputs the resulting magnetic field on a given grid in cylindrical coordinates $\{R, Z, \phi\}$ [12].

3.3 DESCUR

The DESCUR code[6] uses a steepest decent algorithm to find an optimized Fourier representation of a given curve on a surface inside $\mathbb{R}^3$ with a condensed spectrum of the poloidal mode number m. This improves the radial mesh convergence in the calculation of MHD equilibria [23].

A closed curve on a flux surface at fixed toroidal angle ϕ_0 parameterized by the poloidal angle θ is given by its Fourier series as

$$x = \sum x_{mn} \cos(m\theta + n\phi_0) \tag{3.2a}$$

$$y = \sum y_{mn} \sin(m\theta + n\phi_0) \tag{3.2b}$$

with local Cartesian coordinates $x = R - R_0$ and $y = Z - Z_0$ where R_0 and Z_0 define the minor axis of the cylindrical coordinate system $\{R, \phi, Z\}$. This representation of the curve is

[5] Source code can be found in [22].
[6] Source code can be found in [22].

not unique, because the poloidal angle as monotonic increasing function of the arc length can be compressed and stretched what leads to under determination of eq. (3.2). This degree of freedom is used by defining a measure of the spectral extent and add the additional constraint to minimize it. With the definition of a power spectrum of the curve $S_p(m)$ in eq. (3.3a) the applied quantified measure of the spectral extent is given by the q-moment according to eq. (3.3b).

$$S_p(m) = m^p \sum_n \left(x_{mn}^2 + y_{mn}^2 \right) \tag{3.3a}$$

$$M(p,q) = \frac{\sum_{m=1} m^q S_p(m)}{\sum_{m=1} S_p(m)} \quad \text{for } q > 0 \tag{3.3b}$$

The minimization of eq. (3.3b) is obtained by variation with the constraint for the curve not to depart the flux surface. This constraint can be expressed with a function $I(\theta, \phi)$ leading to $\delta M = 0 \leftrightarrow I(\theta, \phi) = 0$, what needs to be solved numerically [23].

In practice the original curve is approximated by its truncated Fourier series. Thus a least square fit through minimization of the curve energy W_c, here defined by the mean square difference between prescribed curve points $\{x_i, y_i\}$ and the Fourier series evaluated at parametric points θ_i, according to

$$W_c = \frac{1}{2} \sum_i \left\{ [x(\theta_i) - x_i]^2 + [y(\theta_i) - y_i]^2 \right\} \tag{3.4a}$$

$$W_T = W_c + \epsilon M \tag{3.4b}$$

is performed. The constrain of minimizing the spectral extent M is added in (3.4b) with a weighting factor ϵ to balance the contributions of reducing the spectral extent and the fitting to the curve. Finding the minimum of (3.4b) needs to fulfill the requirement $I = 0$ from above. This problem is numerically solved by applying a so-called penalty method to solve constrained optimization problems. In this method a constrained optimization problem is expressed as iteration of unconstrained optimizations [24]. For the iteration scheme a steepest decent algorithm is applied along the gradient $-\vec{\nabla} W_T$ [23].

3.4 PARVMEC (NEMEC)

PARVMEC is a parallelized version of the NEMEC code and uses the same physical algorithm to find an equilibrium state of the plasma by minimizing its energy [12]. Therefore the names NEMEC[7] and PARVMEC are used interchangeably in this work by always referring to the parallelized version PARVMEC. In this section the physical context is described and figure 3.3 shows the basic structure of the implementation. Only those parts of the code are described, which are relevant to this work[8].

NEMEC finds a solution of the static equilibrium equations of the ideal MHD picture given by

$$\vec{F} = -\vec{j} \times \vec{B} + \vec{\nabla} p \tag{3.5a}$$
$$\vec{\nabla} \times \vec{B} = \mu_0 \vec{j} \tag{3.5b}$$
$$\vec{\nabla} \cdot \vec{B} = 0 \tag{3.5c}$$

with the residual force $\vec{F} = 0$ in the equilibrium state. The static equilibrium is obtained from the full single fluid ideal MHD equations by neglecting flow and time dependent quantities [25], see section 2.1. One of the coordinate systems NEMEC uses is the flux coordinate system given by $\vec{\alpha} = \{\rho, \theta^*, \zeta\}$ as introduced in section 2.2, with the straight field line angle

$$\theta^* = \theta + \lambda \tag{3.6}$$

and the parameter λ to straighten the field lines in a flux surface[9]. The contravariant representation of the magnetic field in this system is

$$\begin{aligned} \vec{B} &= \vec{\nabla}\zeta \times \vec{\nabla}\chi + \vec{\nabla}\Phi \times \vec{\nabla}\theta^* \\ &= B^\theta \vec{e}_\theta + B^\zeta \vec{e}_\zeta \end{aligned} \tag{3.7}$$

with the poloidal flux $2\pi\chi$ and the toroidal flux $2\pi\Phi$. This representation already includes the restrictions $\vec{B} \cdot \vec{\nabla} p = 0$ and $\vec{\nabla} \cdot \vec{B} = 0$ from the ideal MHD equations [25].

Considering (3.7) in (3.5a) it can be seen, that there are only two independent components of the vector $\vec{F}$. This linear dependence is used to define a toroidal coordinate system $\vec{x} = \{R, \lambda, Z\}$, where the standard toroidal angle ϕ is replaced by λ. This third degree of freedom is identified with the straight field line parameter λ and is used to improve convergence. The R- and Z- component are needed to evaluate the independent components of the force balance $\vec{F} = 0$, as described in the following [25].

[7] As described in figure 5.1 NEMEC consists of the codes NESTOR and VMEC.
[8] Source code can be found in [22].
[9] This is a aimed choice for $\lambda = f(\rho, \theta, \zeta)$ in eq. (2.6) to transform the coordinate system in a way, that field lines are described by eqs. for straight lines in these coordinates. A derivation can be found in [10].

Fixed-boundary.

The energy functional for a fixed-boundary, that is varied, is the sum of magnetic and thermal plasma energy

$$W = \int \left(\frac{B^2}{2\mu_0} + \frac{p}{\gamma - 1} \right) |\sqrt{g}| \, d^3\alpha \tag{3.8}$$

with the adiabatic coefficient γ. The plasma is going to evolve to the minimum energy state, which is found by assuming adiabatic closure of the plasma while moving the fluid to minimize eq. (3.8). Thereby all elements of the fluid are considered isentropic [9].

Starting again with a standard toroidal coordinate system $\vec{x} = \{x_1, x_2, x_3\} = \{R, \phi, Z\}$ the variation is mathematically performed by assuming a time parameter in the coordinates of the flux surfaces $\vec{x} = \{R(t), \phi(t), Z(t)\}$ and also in the straight field line parameter $\lambda = \lambda(t)$. When this time parameter is varied the change in the plasma energy is given by

$$\begin{aligned} \dot{W} = &- \int F_i \dot{x}_i d^3\alpha - \int F_\lambda \dot{\lambda} d^3\alpha - \int_{\rho=1} |\sqrt{g}| \frac{\partial \rho}{\partial x_i} \left(\frac{B^2}{2\mu_0} + p \right) \dot{x}_i d\theta d\zeta \\ &= 0 \quad \text{(in equilibrium)} \end{aligned} \tag{3.9}$$

with implied Einstein summation over roman indices and forces given by

$$\begin{aligned} F_i = &- \frac{\partial}{\partial \alpha_j} \left[|\sqrt{g}| \frac{\partial \alpha_j}{\partial x_i} \left(\frac{B^2}{2\mu_0} + p \right) \right] + \frac{1}{\mu_0} |\sqrt{g}| \, \vec{\nabla} \cdot [(\Lambda_i \vec{B} \cdot \vec{\nabla} x_i) \vec{B}] \\ &+ \delta_{i1} \frac{\left|\sqrt{g}\right|}{R} \left(\frac{B^2}{2\mu_0} + p - \frac{R^2 (\vec{B} \cdot \vec{\nabla}\phi)^2}{\mu_0} \right), \quad \Lambda_1 = \Lambda_3 = 1, \Lambda_2 = R^2 \end{aligned} \tag{3.10a}$$

$$F_\lambda = \frac{\Phi'}{\mu_0} \left(\frac{\partial B_\zeta}{\partial \theta} - \frac{\partial B_\theta}{\partial \zeta} \right) \tag{3.10b}$$

The last term of eq. (3.9) on the right hand side is the energy change due to a moving boundary and can therefore be neglected for fixed boundaries. It is now chosen to identify the toroidal angle ϕ with the magnetic coordinate ζ, thus $\phi = \zeta$. Consequently the corresponding Jacobian $\sqrt{g}$ for the transition from magnetic coordinates $\vec{\alpha} = \{\rho, \theta, \zeta\}$ to toroidal coordinates $\vec{x} = \{R, \phi = \zeta, Z\}$ is reduced to two dimensions as

$$\sqrt{g} = RG \tag{3.11a}$$

$$G = \frac{\partial R}{\partial \theta} \frac{\partial Z}{\partial \rho} - \frac{\partial R}{\partial \rho} \frac{\partial Z}{\partial \theta} \tag{3.11b}$$

The force component F_ϕ can now be omitted, because with $\phi = \zeta$ the two independent force components of eq. (3.5a) are linear combinations of F_R and F_Z in eq. (3.10). Therefore

the equivalence of solving the static equilibrium equations (3.5) for a fixed-boundary and the variation formulation with solution $F_R = F_Z = 0$ can be seen [25].

The equation $F_\lambda = 0$ for solving eq. (3.9) is dependent on $F_R = F_Z = 0$, since there are only two independent MHD force components in eq. (3.5a). This under determination is resolved by introducing a constraint to minimize the spectral extent, which is described in two steps. First, λ is now used as a coordinate in the former mentioned coordinate system $\vec{x} = \{R, \lambda, Z\}$. In these coordinates the force equations are given by

$$\begin{aligned} F_R =& \frac{\partial}{\partial\rho}\left(\frac{\partial Z}{\partial\theta}P\right) - \frac{\partial}{\partial\theta}\left(\frac{\partial Z}{\partial\rho}P\right) + \frac{1}{\mu_0}\left(\frac{\partial}{\partial\theta}(B^\theta b_R) + \frac{\partial}{\partial\zeta}(B^\zeta b_R)\right) \\ &+ G\left(\frac{P}{R} - \frac{(RB^\zeta)^2}{\mu_0}\right) \end{aligned} \tag{3.12a}$$

$$F_Z = -\frac{\partial}{\partial\rho}\left(\frac{\partial R}{\partial\theta}P\right) + \frac{\partial}{\partial\theta}\left(\frac{\partial R}{\partial\rho}P\right) + \frac{1}{\mu_0}\left(\frac{\partial}{\partial\theta}(B^\theta b_Z) + \frac{\partial}{\partial\zeta}(B^\zeta b_Z)\right) \tag{3.12b}$$

$$F_\lambda = \frac{\Phi'}{\mu_0}\left(\frac{\partial B_\zeta}{\partial\theta} - \frac{\partial B_\theta}{\partial\zeta}\right) \tag{3.12c}$$

with $P = R(p + |B|^2/2\mu_0)$ and $b_i = \sqrt{g}\vec{B}\vec{\nabla}x_i$, according to [25]. Eq. (3.12c) is adopted unchanged from eq. (3.10b) for reference in figure 3.3.

Second, the equations $F_R = F_\lambda = F_Z = 0$ are not solved directly because of numerical reasons [25]. A steepest descent algorithm is applied, which utilises the Fourier representations for the coordinates $\vec{x} = \{R, \lambda, Z\}$ by

$$x_j = \sum_{m,n} X_j^{mn}(\rho)\exp[i(m\theta + n\zeta)] \tag{3.13}$$

with the poloidal and toroidal angles θ and ζ. Using this representation for $\vec{x}$ in eq. (3.9) leads to [12]

$$\dot{W} = -\sum_{m,n}\int (F_j^{mn})^* \dot{X}_j^{mn} dV \quad \text{with} \tag{3.14a}$$

$$F_j^{mn} = \frac{1}{V'}\int\int F_j \exp[-i(m\theta + n\zeta)]d\theta d\zeta \tag{3.14b}$$

In [25] it is shown for a fixed-boundary, that the path of the steepest descent is described by

$$\dot{X}_j^{mn} = F_j^{mn} \tag{3.15a}$$

$$\dot{W} = -\sum_{m,n,j}\int \left|F_j^{mn}\right|^2 dV \tag{3.15b}$$

with the associated energy reduction in eq. (3.15b), where $\dot{W} = 0$ is equivalent to $F_j^{mn} = 0$ for all m, n, j.

Now the additional constraint to minimize the spectral extent of R_j^{mn} and Z_j^{mn} is applied, by means of minimizing the measure M like in DESCUR, section 3.3. The minimization can be expressed as additional constraint forces $F_{R,con}$ and $F_{Z,con}$. When these forces are added and $F_{\lambda,con} = 0$ the equations

$$F_j^{mn} = (F_j + F_{j,con})^{mn} \quad \text{for } j = (R, \lambda, Z)^{10} \tag{3.16}$$

are now independent and define by means of (3.6) a unique poloidal angle [26].

For the steepest decent algorithm NEMEC solves eq. (3.15a) in an iterative manner according to eq. (3.22) in figure 3.3. To improve the convergence of the solution the parabolic differential equations (3.15a) are translated to hyperbolic equations, using a second-order Richardson scheme introducing a critical damping in the iteration [25].

A further limitation that needs to be imposed, while minimizing the energy, is that two flux surface quantities are prescribed. Otherwise one would obtain a state with $\vec{B} = 0$ and $p = 0$, which is the trivial solution for an equilibrium state [9]. NEMEC prescribes the pressure profile, which ensures mass conservation on each flux surface. Additionally the profiles of the radial derivative (w.r.t to ρ) of the poloidal flux χ' and the radial derivative of the toroidal flux Φ' are prescribed [25]. These magnetic profiles are entered externally by specifying the radial derivative of the toroidal plasma current on each flux surface and total plasma current I_{pl}, as well as the toroidal magnetic flux on the plasma edge Φ_{edge}[11].

Free-boundary. Use of NESTOR.

NEMEC can also perform free-boundary calculations, when the plasma is considered to be in a vacuum with a magnetic field $\vec{B}_{vac}$ which is contained inside a conducting wall. Therefore two constraints for the plasma boundary need to be fulfilled. These are the pressure continuity $B^2/2\mu_0 + p = B_{vac}^2/2\mu_0$ and the Neumann constraint $\vec{B} \cdot \vec{n}_{pl} = 0$, with the plasma surface normal vector $\vec{n}_{pl}$. A free-boundary equilibrium is computed by a comparable approach to the fixed-boundary described above by including the constraints in the energy functional. Eq. (3.8) becomes then

$$W = W_{pl} - W_{vac} = \int_{plasma} \left(\frac{B^2}{2\mu_0} + p \right) |\sqrt{g}| \, d^3\alpha - \int_{vacuum} \frac{B_{vac}^2}{2\mu_0} |\sqrt{g}| \, d^3\alpha \tag{3.17}$$

with the magnetic vacuum field expressed by a scalar magnetic potential $\vec{B}_{vac} = \vec{\nabla}\tilde{\nu}$ [25]. The same variation as for the fixed-boundary case gives now

[10] In the implementation the computation of the total MHD and constraint force is performed inside the Fourier transformation and uses a different summation scheme, based on derivative terms [25] [22].

[11] For NEMEC it would also be possible to prescribe the q-profile instead of the toroidal current profile, but the baseline ASTRA simulation [14] prescribed the q-profile and therefore reaching the same q-profile, which is a topological invariant in the absence of time evolution, is used as a consistency check in this work [9].

$$\begin{aligned}\dot{W} = &- \int F_i \dot{x}_i d^3\alpha + \frac{1}{\mu_0}\int_{vacuum} \dot{\tilde{\nu}} F_{\tilde{\nu}} d^3x \\ &- \int_{\rho=1} \left[|\sqrt{g}| \frac{\partial \rho}{\partial x_i} \left(\frac{B^2}{2\mu_0} + p - \frac{\left|\vec{\nabla}\tilde{\nu}\right|^2}{2\mu_0} \right) \right]_{\rho=1} \dot{x}_i d\theta d\zeta \\ &- \frac{1}{\mu_0}\left(\int_{\rho=1} \dot{\tilde{\nu}} \vec{B}_{vac} \cdot d\vec{S}_\rho - \int_{wall} \dot{\tilde{\nu}} \vec{B}_{vac} \cdot d\vec{S} \right)\end{aligned} \tag{3.18}$$

The second line represents the pressure jump at the plasma edge and must vanish because of the constraint of pressure continuity. The third line contains surface integrals with the terms $\vec{B}_{vac} \cdot d\vec{S}$, which also need to vanish because of the Neumann constraint. Thus the constraints are fulfilled and an additional force is

$$F_{\tilde{\nu}} = -\vec{\nabla} \cdot \vec{B}_{vac} \tag{3.19}$$

The corresponding path of the steepest decent for this force, in analogy to the fixed-boundary case, is $\dot{\tilde{\nu}} = F_{\tilde{\nu}}$. The other forces F_i with $i = (R, \lambda, Z)$ are given in eq. (3.12), where at the boundary the values for the Fourier amplitudes $\{R_b^{mn}, Z_b^{mn}\}$ are now not prescribed, but $P_b = R_b(|B_{vac,b}|^2 / 2\mu_0)$, with the vacuum induction field at the plasma boundary $\vec{B}_{vac,b}$ is applied [25, 27].

Instead of using a steepest decent method for $\tilde{\nu}$ in NEMEC, the vacuum induction field is computed with the NESTOR code. This code uses a similar representation of the vacuum field to $\vec{B}_{vac} = \vec{\nabla}\tilde{\nu}$, but the field produced by external coils and plasma currents, $\vec{B}_0$, is separated to

$$\vec{B}_{vac} = \vec{B}_0 + \vec{\nabla}\nu \tag{3.20}$$

The field $\vec{B}_0$ is kept constant during an equilibrium computation and the scalar potential needs to satisfy the Laplace equation $\Delta\nu = 0$. Furthermore the normal derivative of the scalar potential has to fulfill $\partial\nu/\partial n = -\vec{B}_0 \cdot \vec{n}_{pl}$ at the plasma boundary, with again the plasma surface normal vector $\vec{n}_{pl}$. Therefore an integral equation for ν, using Greens third identity, can be derived as

$$\nu(\vec{x}) + \frac{1}{2\pi}\int d\Sigma'_{pl} \frac{\partial G(\vec{x}, \vec{x'})}{\partial n'} \nu(\vec{x'}) = \frac{1}{2\pi}\int d\Sigma'_{pl} G(\vec{x}, \vec{x'}) \frac{\partial \nu(\vec{x'})}{\partial n'} \tag{3.21}$$

with points $\vec{x}$ and $\vec{x'}$ on the plasma boundary Σ_{pl} and the Green's function $G(\vec{x}, \vec{x'}) = 1/\left|\vec{x} - \vec{x'}\right|$. This integral equation is solved by NESTOR in Fourier space [27].

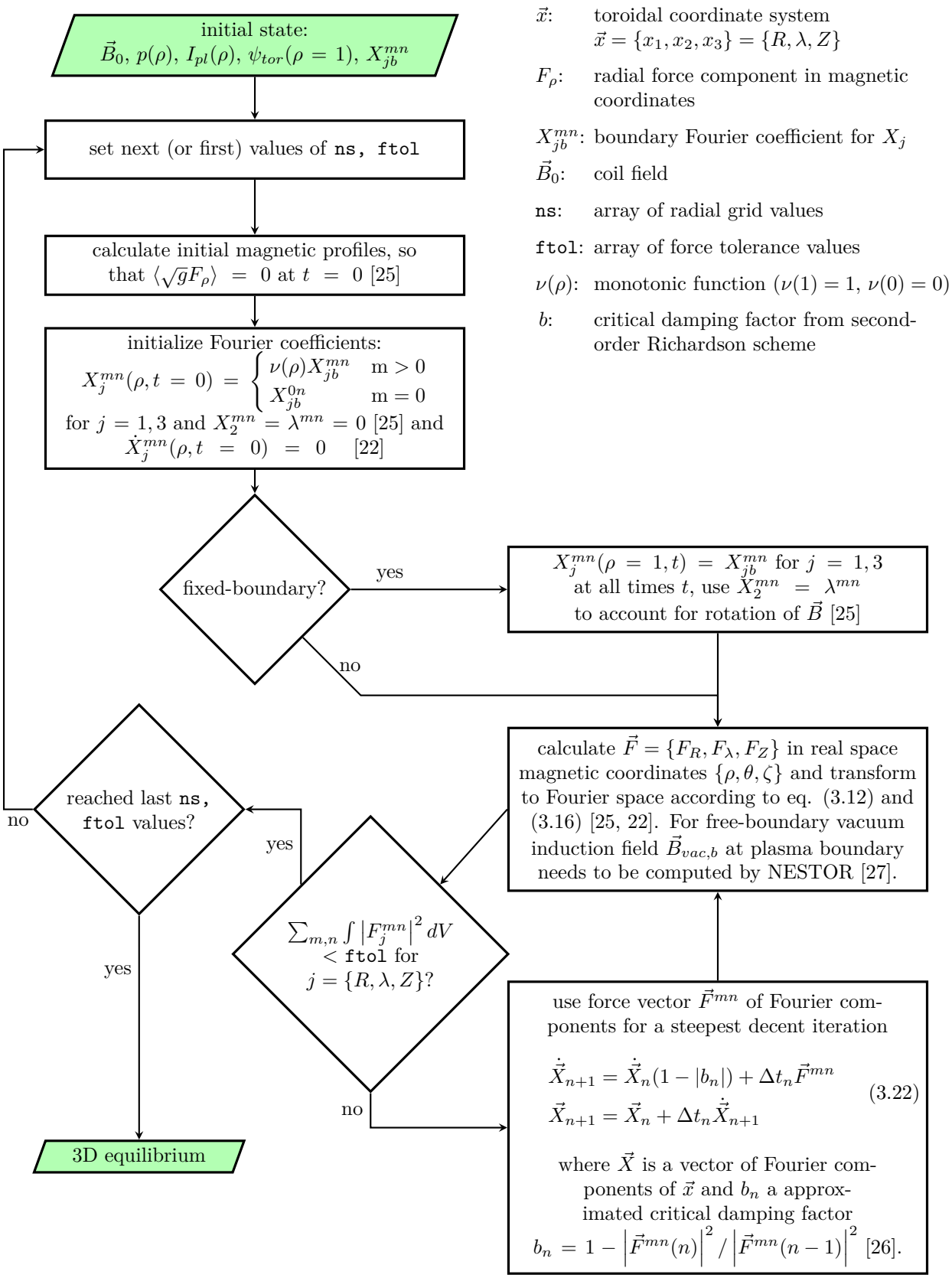

Figure 3.3: Visualization of the basic NEMEC energy minimization algorithm used for this work with aid of [25] [26] [27] [22]. The implemented algorithm deviates in details in favour of improved numerical methods.

4 DEMO baseline scenarios and coil system

4.1 Plasma scenarios supplied by ASTRA simulations

4.1.1 L-mode

The plasma scenarios in this thesis are provided by transport simulations executed within the scope of [14], where the TGLF model for the transport coefficients according to section 3.1.1 and the 2D equilibrium solver SPIDER, as explained in section 3.1.2 are coupled in ASTRA simulations. The engineering parameters given in table 4.1 are part of the input for these ASTRA simulations, as explained in figure 3.2. The transport simulations of [14] represent the latest physics scenarios and are referred in this thesis as provision study.

Major radius R_0	9 m
Separatrix elongation κ_{sep}	1.77
Separatrix triangularity δ_{sep}	0.39
Plasma current I_{pl}	17.75 MA
On-axis toroidal induction field B_0	5.85 T
Truncated separatrix safety factor q_{sep}	3.96
Greenwald density n_{GW}	$7.2 \cdot 10^{19}\,\mathrm{m}^3$
Plasma volume V	$\approx 2635\,\mathrm{m}^3$
Helium concentration c_{He}	8 %
Target fusion power $P_\alpha + P_n$	2 GW
Target pulse time	7200 s
Available auxiliary heating power P_{aux}	130 MW

Table 4.1: Engineering parameters of EU-DEMO 2018 baseline used as input parameters in the ASTRA simulations of [14]. These ASTRA simulations provide the L-mode and H-mode scenarios for this thesis and therefore the results presented are related to the same engineering parameters. Some quantities refer to the separatrix, which is a curve at the plasma boundary. The separatrix is the curve, which separates confined and unconfined field lines. It is marked in figure 4.1 (b).

In [14] the feasibility of the L-H Transition in a purely **E**lectron **C**yclotron **R**esonant **H**eated (ECRH) DEMO tokamak is investigated. Therefore, the L-mode scenario for this thesis is heated by 50 MW ECRH. Considering the time dependent current in the central solenoid inducing the plasma current, the L-mode is located in a state of constant plasma current after the ramp up phase, what is called the flat top. An electron density at the boundary of $2 \cdot 10^{19}\,\mathrm{m}^{-3}$ is used as further input parameter for the L-mode simulation. The impurities of the D-T-plasma are assumed to consist of 8 % helium of the 2018 baseline, together with 40 ppm tungsten. In [14] the boundary condition $T_e(\rho = 1) = T_i(\rho = 1) = T_{e,sep}$ is imposed for the electron and ion temperatures at the separatrix, where $T_{e,sep}$ is computed by a 2-point-model. The resulting 2D equilibrium of SPIDER has 71 radial grid points and the 'in-ASTRA'-time is incremented in steps of 5 ms. TGLF is called every 25 ms, to recompute the turbulent transport coefficients [14].

The physical quantities of the L-mode scenario, used in NEMEC to compute the 3D nested flux surfaces, are the pressure profile $p(\rho)$, the plasma current profile $I_{pl}(\rho)$, the total toroidal flux Φ_{edge}, the shape of plasma boundary and the position of the magnetic axis. The profiles are expressed as a function of the square root of the normalized toroidal flux $\rho = \sqrt{\Phi/\Phi_{edge}}$. Together with the prescribed 2D axisymmetric boundary of the plasma, supplemented with the inner flux surfaces computed by SPIDER and the position of the magnetic axis, they are depicted in figure 4.1. For a fixed-boundary simulation in NEMEC the $\{R, Z\}$ coordinates of the axis are taken as initial values and can change while evolving to minimum energy state. The same is valid for the plasma boundary in a free-boundary NEMEC simulation.

The ASTRA output file does not contain the pressure and plasma current directly. Hence, they are computed by

$$p = n_e T_e + \sum_i n_i T_i + p_{fast} \tag{4.1a}$$

$$I_{pl} = \frac{1}{2\pi R_0} \int_0^\rho V' j_{tor} d\rho \tag{4.1b}$$

according to [16]. The summation over the ions for the pressure profile includes the thermal contribution of impurities helium and tungsten. Furthermore the pressure profile contains besides the density and temperature of electrons and ions the fast-ion pressure p_{fast}. This pressure contribution arises from non-thermal ions and is substantial in the core region. The plasma current profile needs to be integrated over the radial derivative (w.r.t to ρ) of the volume inside a flux surface V' and the toroidal current density j_{tor}. As described in section 3.4, NEMEC does not change the pressure and plasma current profile and considers them as prescribed. The total toroidal flux Φ_{edge} is also a conserved quantity in NEMEC simulations, but is not directly available in ASTRA output files. The computation of the value of Φ_{edge} for the coupling of ASTRA to NEMEC is described in section 5.2. For the L-mode a value of $\Phi_{edge} = 272\,\mathrm{Wb}$ is computed in this work.

In figure 4.1 (a) it is shown, that the value for the plasma current $I_{pl}(\rho = 1) = 20.97\,\mathrm{MA}$ is above the engineering value of EU-DEMO 2018 baseline in table 4.1. This is because the q-profile and not the plasma current is prescribed in the ASTRA simulations in the scope of [14]. The current density inside the plasma is computed, to solve the Grad-Shafranov-eq., as explained in section 3.1.2.

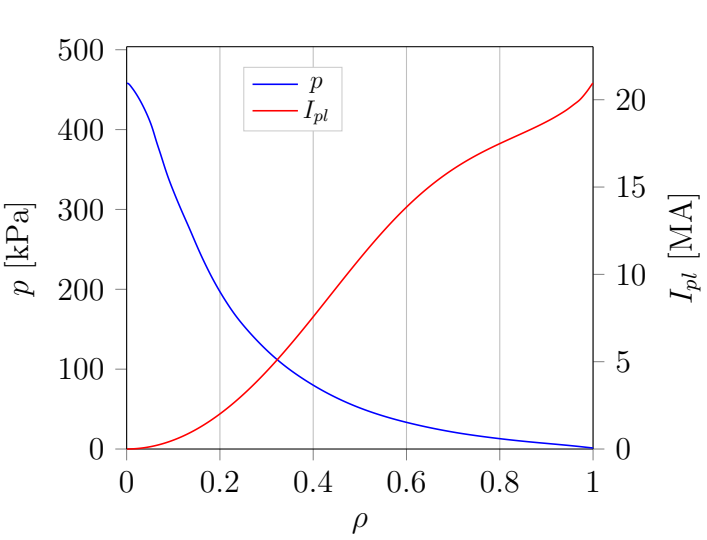

(a) L-mode profiles

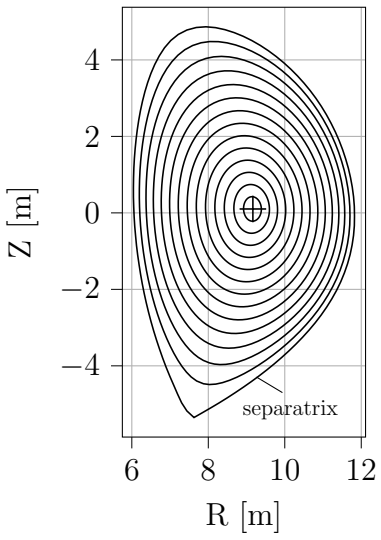

(b) L-mode flux surfaces

Figure 4.1: (a) ASTRA profiles of the L-mode according to eq. (4.1) with respect to radial grid variable ρ, computed in ASTRA transport simulations in the scope of [14]. These are preprocessed as described in section 5.2 into an input format for NEMEC and kept constant during the scope of this work for L-mode simulations. (b) Prescribed plasma boundary according to EU-DEMO 2018 baseline applied in ASTRA simulations with inner flux surfaces computed by SPIDER in the context of [14]. The magnetic axis and the boundary serve as initial values for NEMEC simulations and can vary within this work.

4.1.2 H-mode

The developed ASTRA simulation code of [14] is used externally to this work to supply a DEMO H-mode scenario. Thereby a comparable procedure as for the L-mode in the previous section is used. The H-mode is modeled by including a characteristic H-mode pedestal in the prescribed pressure profile, according to [28]. It is combined with a heating power of 50 MW ECRH and an electron density in the pedestal top of $n_{ped} = 6 \cdot 10^{19}\,\mathrm{m}^{-3}$. For the impurities 8 % helium and 40 ppm tungsten, proportional to the electron density, are assumed. In combination with the engineering parameters in table 4.1, a self consistent plasma scenario is computed in ASTRA simulations and the results are provided for this thesis. These ASTRA simulations are carried out in the context of [14], as for the L-mode.

Since both plasma scenarios are processed in this work with the same code system the relevant quantities for NEMEC are again the pressure profile $p(\rho)$, the plasma current profile $I_{pl}(\rho)$, the total toroidal flux Φ_{edge}, the geometry of the plasma boundary and the position of the magnetic axis. The pressure and the plasma current profile are computed according to eq. (4.1) and depicted together with the plasma boundary and magnetic axis in figure 4.2. As for the L-mode the computation of the total toroidal flux Φ_{edge} is described in section 5.2 and gives for the H-mode a value of $\Phi_{edge} = 271\,\mathrm{Wb}$.

One can observe in figure 4.2 (a) that the plasma current exceeds the value from the EU-DEMO baseline 2018 in table 4.1 with a value for the H-mode of $I_{pl}(\rho = 1) = 21.46\,\mathrm{MA}$. The reason is the same as for the L-mode, that the q-profile is prescribed and the plasma current

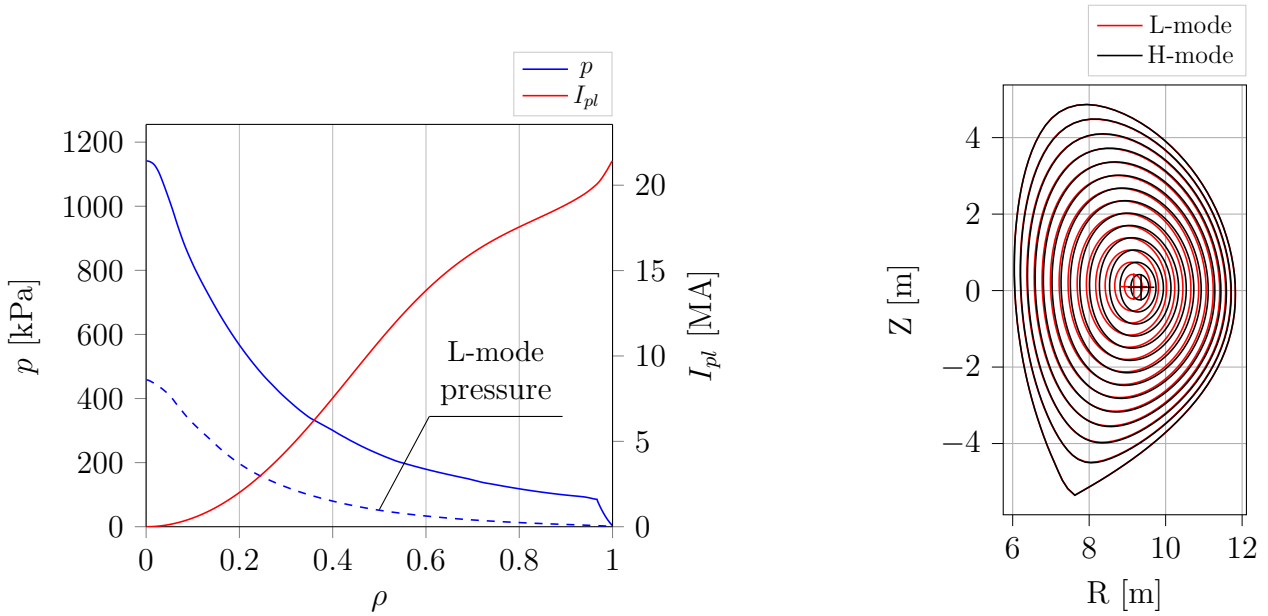

(a) H-mode profiles

(b) H-mode flux surfaces

Figure 4.2: (a) H-mode profiles computed with ASTRA simulations with respect to radial grid variable ρ. The ASTRA simulation use the same procedure as the L-mode simulation and therefore the profiles are given by eq. (4.1) . The significant difference between the H-mode and the L-mode is visualized by comparison to the dashed pressure profile of the L-mode. A steep rise of the pressure profile near the edge at $\rho = 1$ is a result of a transport barrier, see section 2.4. These profiles are prescribed in following H-mode NEMEC simulations during the scope of this work. (b) Prescribed plasma boundary according to EU-DEMO 2018 baseline applied in ASTRA simulations with inner flux surfaces computed by SPIDER. The magnetic axis is shifted radially outwards by 0.19 m compared to the L-mode due to the changed pressure profile.

is computed to solve the Grad-Shafranov-eq. in SPIDER.

As described in section 2.4 the H-mode scenario is seen as the operational state for DEMO due to the high energy confinement resulting from the transport barrier. The presented H-mode scenario is expected to achieve 600 MW of fusion power, what is below the stated value of 2 GW of the engineering parameters. The improvements are ongoing while this thesis is written.

4.2 Coil system and ferromagnetic inserts

In figure 4.3 the coil system for producing the vacuum induction field $\vec{B}_{vac}$ is presented. For identification of coil currents all poloidal field coils and all segments of the central solenoid are labeled. These coil currents are used to create the vertical field and were adjusted for the plasma shaping, see section 5. The geometry of the PF coils and the central solenoid is based on the physics scenario 2019 of EUROfusion. For the toroidal field there are 16 D-

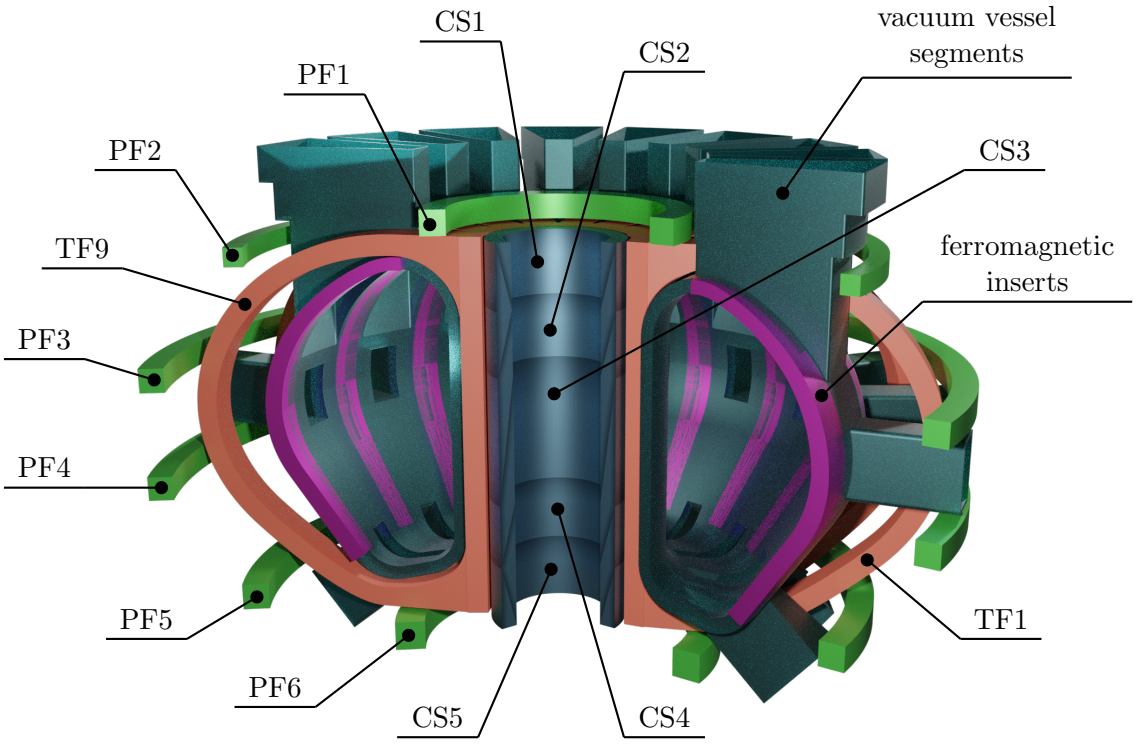

Figure 4.3: Sectional view of the applied DEMO coil system for this thesis, including ferromagnetic inserts installed into the segments of the vacuum vessel. The vacuum vessel is made up of 16 segments in the toroidal direction and each segment has three ports. Between these ports the toroidal field coils (TF coils) are located, with ferromagnetic inserts (FI) underneath each TF coil. The volume of each ferromagnetic insert is divided symmetrically around the connection surface of the two segments of the vacuum vessel. There are 16 TF coils in total, which are enumerated counter clockwise viewed from above. Furthermore poloidal field coils (PF coils) and the segments of the central solenoid (CS) are depicted.

shaped coils which create the toroidal field ripple due to their toroidal spacing. As well as the geometry of the vacuum vessel, they are based on the EU-DEMO baseline 2017, where most of the engineering work was carried out. The ferromagnetic inserts are created based on the geometry of the vacuum vessel. These ferromagnetic inserts are passive elements and interact with the field produced by the coils by aligning existing microscopic magnetic moments along the field they are exposed to. Thus, the toroidal field inside the ferromagnetic inserts is enhanced, while, on the other hand, the field outside the ferromagnetic inserts at the plasma boundary is reduced. Therefore the toroidal field ripple is reduced, as explained in section 5.3.3.

5 Coupling of the code system

5.1 Outline of the code system and applied workflow for ripple studies

A code system has been developed to process output from ASTRA simulations into 3D coordinates of nested flux surfaces, computed by NEMEC. The 2D equilibrium computed by the equilibrium solver SPIDER, as part of the ASTRA simulations, is coupled with a realistic coil system containing a finite number of toroidal field coils and therefore the toroidal field ripple. Thereby existing simulation and computation codes according to section 3 are utilized and connected together by newly developed codes. Besides NEMEC, MAKEGRID and DESCUR also ASTRA is considered as an existing code. This is because the creation of the actual transport simulation by using the ASTRA environment is done in the provision study [14], as described in section 4.1. Newly developed are the codes PIGEN (**P**ARVMEC **I**nput **GEN**erator)and MIGEN (**M**AKEGRID **I**nput **GEN**erator). Their integration in the overall code system is shown in figure 5.1.

This code system is applied in a workflow, consisting of three major steps. Each of these steps is carried out first for the L-mode and afterwards for the H-mode.

1. *2D fixed-boundary simulation in NEMEC.*
   The ASTRA output file for the corresponding plasma scenario is translated to a NEMEC input file by using PIGEN. The relevant tasks PIGEN needs to perform are described in section 5.2. In the ASTRA simulations in the scope of [14] for this work the q-profile is prescribed, but it evolved in NEMEC. Therefore a first consistency check is carried out by reaching the same q-profile in the NEMEC simulation.
2. *2D free-boundary simulation in NEMEC.*
   The next step consists of using MIGEN to create a MAKEGRID input file, based on geometry of the poloidal field coils and the central solenoid, to produce a 2D axisymmetric vacuum induction field. This field is then used in a 2D free-boundary NEMEC simulation. Because the plasma boundary is prescribed in [14], the values of the coil currents need to be adjusted to reproduce the boundary, see section 5.3.1 for details.
3. *3D free-boundary simulation in NEMEC.*
   The last step of the workflow takes the toroidal field coils and ferromagnetic inserts into account to compute a 3D vacuum induction field with MAKEGRID. Again MIGEN is used to create the corresponding input file for MAKEGRID, as described in section 5.3.2 and 5.3.3. The resulting 3D vacuum induction field is then applied in 3D free-boundary NEMEC simulations to evaluate the plasma response and the impact of the ferromagnetic inserts.

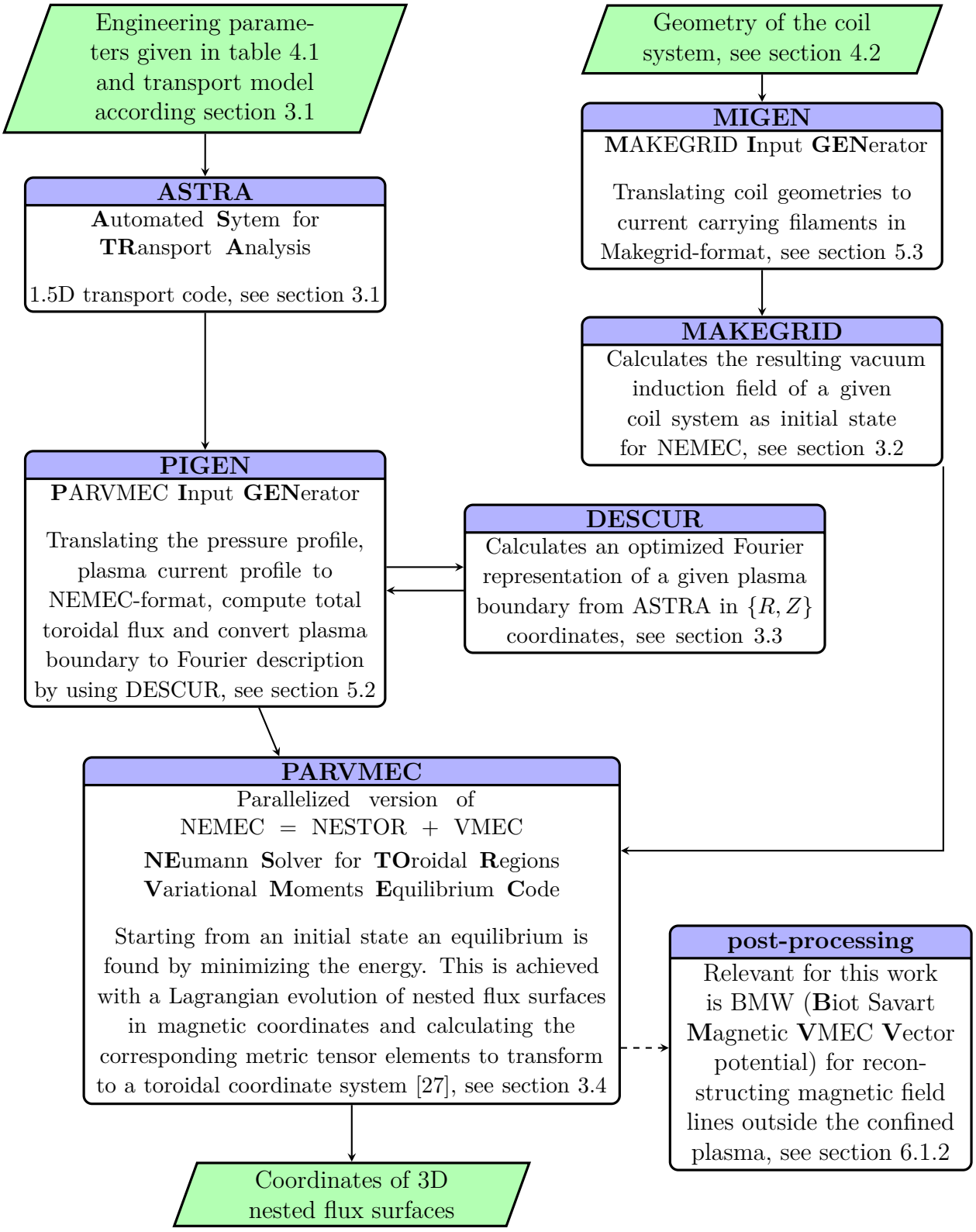

Figure 5.1: Outline of the code system to process a 2D axisymmetric equilibrium of an L-mode and an H-mode scenario to 3D nested flux surfaces under consideration of the toroidal field ripple. The relevant L-mode and H-mode are described in section 4.1. With the resulting 3D coordinates the plasma response to the toroidal field ripple is investigated in section 6.

5.2 Preprocessing of ASTRA output

The output files of ASTRA simulations can not be loaded directly into NEMEC simulations, although the physical quantities are available. Besides formatting of an input file, there are four major tasks to be done. Each of these is described below, together with an investigation of the q-profile convergence. In this work these four tasks were automatized and combined in a tool named PIGEN.

Pressure profile.

The ASTRA output file contains several pressure contributions, depending on the applied modules. The ones that are taken into account in this work are the pressure of thermal electrons, thermal ions and the fast ion contribution, as given in eq. (4.1a). For each flux surface a value for the pressure exists. In ASTRA flux surfaces use the square root of the normalized toroidal flux $\rho = \sqrt{\Phi/\Phi_{edge}}$ as radial coordinate and can therefore take values between $[0, 1]$. NEMEC on the other hand uses s, the normalized toroidal flux as radial magnetic coordinate $s = \Phi/\Phi_{edge}$. The relation between the two different radial grid variables is

$$s = \rho^2 \tag{5.1}$$

In PIGEN the values for the pressure are unchanged, just the corresponding grid position is squared. Additionally the radial grid in ASTRA skips the point at $\rho = 0$. For NEMEC the pressure profile is thus linearly extrapolated to the axis. As one can see in the pressure profiles of the L-mode (figure 4.1) and H-mode (figure 4.2) this is an appropriate assumption.

Plasma current profile.

The plasma current profile $I_{pl}(s)$ is used in this work as second input profile for NEMEC. In NEMEC the plasma current profile is passed as radial derivative of the normalized plasma current and the absolute value of $I_{pl}(s = 1) = I_{pl}(\rho = 1)$. The needed absolute values are given for L-mode and H-mode in sections 4.1.1 and 4.1.2. For the computation of the radial derivative of the plasma current profile the values of the ρ-grid in ASTRA need to be translated to a s-grid according to eq. (5.1). Thereby numerical issues arise, both on the axis ($\rho = s = 0$) and at the **L**ast **C**losed **F**lux **S**urface (LCFS at $\rho = s = 1$), as figure 5.2 shows. On the left side of this figure it is shown, that a small unphysical drop in the plasma volume computed by SPIDER between the value at $\rho = 1$ and the previous one leads to a substantial drop in the radial derivative. This is caused by the sensitivity of the applied first order finite differences approach for the computation of $dV/d\rho$, due to small denominators. The applied solution is to replace the last value of the volume by a linear extrapolation. The second numerical peak is near the axis at $s = 0$ in the dV/ds-curve. While keeping the values for the volumes of flux surfaces V, the differences in the coordinate s between two neighboring flux surfaces is reducing quadratic, because of eq. (5.1). According to eq. (4.1b) the radial derivative of the plasma current is proportional the product of the toroidal current density j_{tor} and the radial derivative of the volume. Therefore the numerical peak in the original curve of dV/ds is also present in the plasma current for NEMEC. To avoid this, again a fit of the radial derivative

of the volume on the s-grid is applied. Near the axis the volume inside a flux surface can be approximated by $V = 2\pi R_0 \cdot \pi r^2 = 2\pi^2 R_0 r^2$, where r is a average minor radius. With $s = \Phi/\Phi_{edge} \propto r^2$ [10] one can see that $V \propto s$. Therefore

$$\lim_{s \to 0} \frac{dV}{ds} = const. \tag{5.2}$$

In SPIDER on the other hand the differences in successive volumes is not decreasing fast enough by translating to the s-grid. This is implemented in PIGEN, by a horizontal fit of the radial derivative of dV/ds to $s = 0$, beginning at a user specified value. The solid lines in figure 5.2 show the curves used for NEMEC simulations in this work.

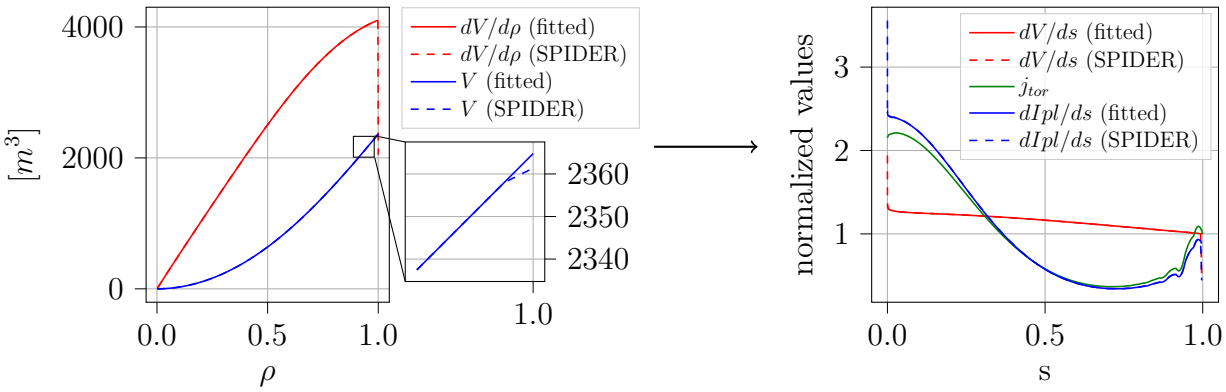

(a) L-mode

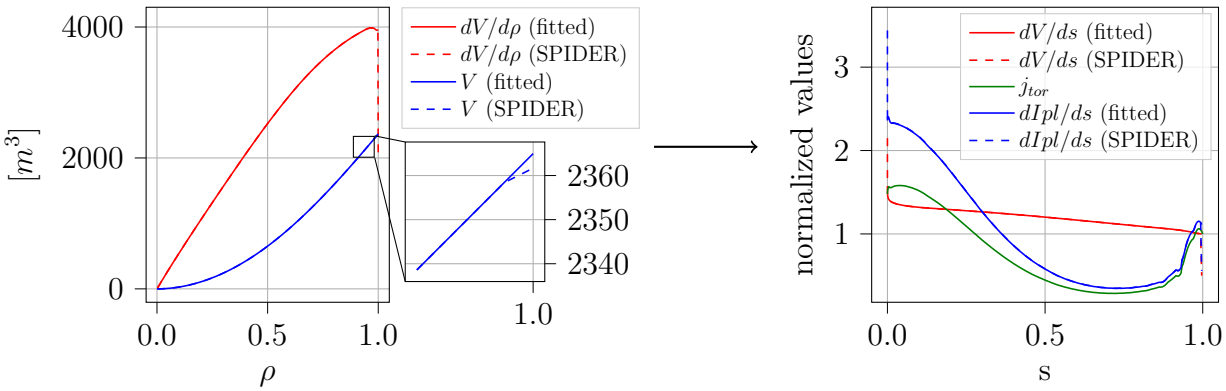

(b) H-mode

Figure 5.2: For L-mode (a) and H-mode (b) on the left side the volume and its radial derivative computed by SPIDER on ρ-grid is shown. As indicated by arrows these quantities are translated to dV/ds for NEMEC, where one can observe that the drop at LCFS in the data of SPIDER impacts both grids. Additionally a second numerical peak at the magnetic axis at $s = 0$ occurs, because of the numerical sensitivity of the applied first order finite differences approach for the computation of dV/ds. The radial derivative of the plasma current dI_{pl}/ds used in NEMEC is proportional to the product of $dV/ds \cdot j_{tor}$, that is why the numerical inaccuracies in dV/ds of the SPIDER data would translate to NEMEC input. The dashed data is taken directly from SPIDER, the solid lines indicate the fitting for passing the data to NEMEC as explained in the text.

Computation of the total toroidal flux.

The total toroidal flux needs to be prescribed as a conserved quantity in NEMEC simulations. In the equilibrium solver SPIDER, implemented into the provided ASTRA simulations of [14], the Grad-Shafranov-eq. for the poloidal flux χ is solved. Between the poloidal and toroidal flux the relation ship $\bar{\iota} = \chi'/\Phi'$ with the rotational transform $\bar{\iota} = 1/q$ (eq. (2.12)) is used to computed the total toroidal flux by

$$\Phi_{edge} = \int_{s=0}^{s=1} \chi' q ds \tag{5.3}$$

where prime denotes the radial derivative with respect to s.

Optimized Fourier representation of the boundary.

As described in section 3.4 NEMEC uses a constraint to reduce the spectral extent of the poloidal mode number m and produce condensed Fourier representations. For this reason the Fourier coefficients for the boundary passed to NEMEC need to fulfill the same constraint. Otherwise boundary layers in the spectral representation can occur [26].

The plasma boundary in the ASTRA output file is given in $\{R, Z\}$ coordinates. These are translated to Fourier coefficients by calling DESCUR, which is based on the same spectral condensation, as explained in section 3.3. This ensures the correct behaviour of the spectral representation in NEMEC simulations near the LCFS. A consequence of the Fourier representation is, that the so-called X-point can not be resolved with a finite number of poloidal harmonics. The X-point can be seen in figure 4.1 (b) as the lowest point (smallest Z-coordinate) of the separatrix, where a kink is located. This has no impact on the investigations in this thesis, but it is used to distinguish in the following discussions the expression separatrix and LCFS. A separatrix is referred to the curve of a plasma boundary with resolved X-point and a LCFS without resolved X-point, because of a finite number of poloidal harmonics.

Convergence of q-profile.

As described in section 3.4, NEMEC needs besides the pressure profile a second profile, which can either be the q-profile or the plasma current profile. In provision study [14], which provides the plasma scenarios, the q-profile is a prescribed flux surface quantity. To perform a consistency check with regard to the preprocessing of the ASTRA output, the plasma current profile is used as a second profile in NEMEC. Therefore, the q-profile is evolving and the simulation is expected to end with the q-profile as originally prescribed in the ASTRA simulations. This consistency check is shown in figure 5.3.

It can be seen in figure 5.3, that there is a deviation of the two q-profiles near $\rho = 0$. Because this quantity is located in the vicinity of the magnetic axis, the influence of the maximum poloidal mode number as numerical parameter in the NEMEC simulations can be neglected. It is expected, that the major influence is the resolution of the radial grid in combination with the force tolerance, see figure 3.3. NEMEC uses a constant grid in the radial coordinate s and hence, the total number of radial grid points needs to be increased to resolve the axis region. As shown in figure 5.4 the value of $q(s = 0)$ in the L-mode takes a value slightly above 0.96. This drop of the q-profile in the vicinity of the magnetic axis has no influence on the

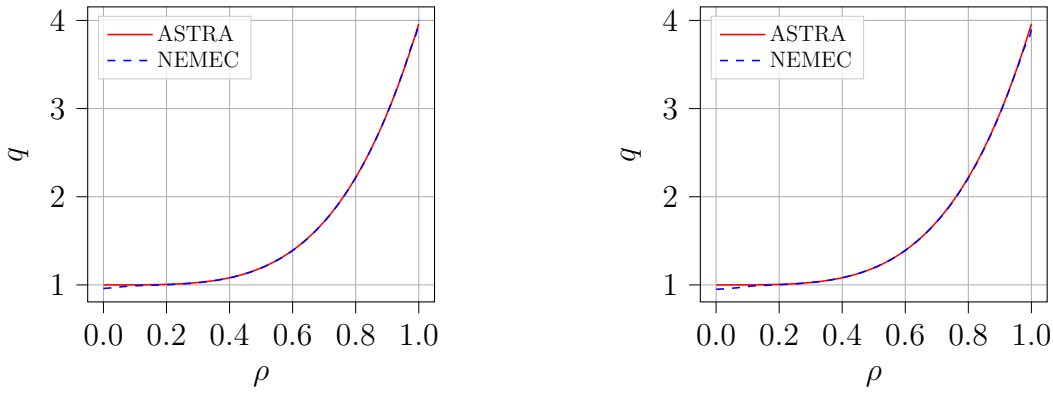

(a) L-mode (b) H-mode

Figure 5.3: The q-profiles of L-mode (a) and H-mode (b) as a result of 2D fixed-boundary NEMEC simulations. The q-profiles are not prescribed in NEMEC and evolve while minimizing the energy of the plasma. For comparison the q-profile of ASTRA are included. One can see that up to difference in the vicinity of the magnetic axis the q-profiles of NEMEC and ASTRA are the same.

results in this work. Besides the numerical resolution in NEMEC the accuracy of SPIDER can be a source of the deviation between the simulation results. SPIDER is intended for rapid simulations in integrated modeling. Furthermore, SPIDER is called just every 5 ms of in-ASTRA time. Therefore, the solutions of NEMEC and SPIDER can be related to slightly different times.

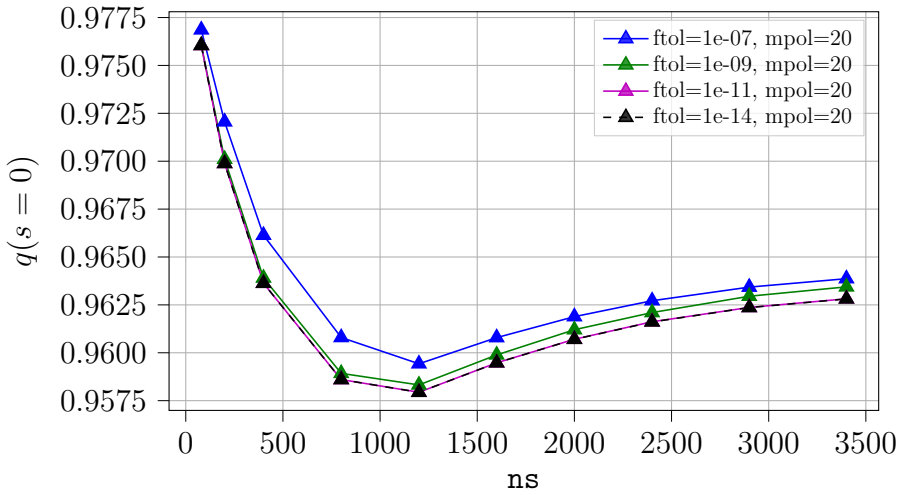

Figure 5.4: On-axis $q(s = 0)$ of the L-mode plasma scenario as a function of numerical parameters `ns` and `ftol`. The maximum poloidal mode number `mpol` used in NEMEC is kept at a numerical efficient value of 20. The force tolerance is converged at a value of `ftol`$=1 \cdot 10^{-11}$. The radial grid points show convergent behaviour even though a value of `ns`=3400 is not fully converged.

5.3 Modelling of the coil system for MAKEGRID

5.3.1 Axisymmetric vacuum induction field. Poloidal field coils and central solenoid

For computing a 2D vacuum induction field the poloidal field coils, as well as the central solenoid segments according to figure 4.3 need to be translated to MAKEGRID input format. MAKEGRID works internally with filaments representing line conductors. The extended spatial cross section of coils needs to be approximated by several windings, where each winding is represented by a closed loop of a line conductor. In order to convert the given geometry of the coils, each coil is first considered to consist of a single line conductor describing the central path along the coil. A cross section is then supplemented and extruded along the path. This modeling of the coils is done by using a code called MIGEN.

For a circular conductor, wound around the torus axis, MAKEGRID uses a representation by a single coordinate in a R-Z-plane. The rotation around the axis is performed implicitly inside MAKEGRID. Therefore, to model an extended cross section a set of points needs to be generated. MIGEN does this, by receiving first the coordinate of the center point of the cross section, which is interpreted as the path of the coil. In a second step the cross section is defined by the linear dimension in the R- and Z-coordinate, together with a maximum distance between neighbouring windings[1]. Based on this maximum distance the needed number of windings in both directions is computed and the windings are positioned equally along the axes. The result of this procedure is depicted in figure 5.5.

Besides the geometry of a coil, the current inside each winding needs to be passed to MAKEGRID. Together with the geometry this value was initially taken from the baseline 2019 scenario of EUROfusion. The usage of MAKEGRID output files for a free-boundary simulation in NEMEC offers the flexibility to adjust the current of each coil by the NEMEC input file. This is enabled, because MAKEGRID stores the vacuum induction field resulting from each coil separately. The overall induction field can then be received by the vector sum, due to the superposition of magnetic fields. As one can see based on eq. (3.1), multiplying the originally applied coil current I_i^{cond} by a constant factor is equivalent to multiplying the resulting field $\vec{B}^{coil}$ of a coil by this factor. This flexibility is implemented in NEMEC by specifying so-called `extcur`-values for each coil. NEMEC multiplies the corresponding coil induction field with the `extcur`-value before computing the vector sum and therefore this is equivalent to using different values for the coil currents in the first place. This feature is utilized in this work to adjust the plasma shape. The initially applied values for the currents of the coils in figure 5.5 result in different plasma boundaries than the ASTRA simulations prescribed, due to the progress from DEMO baseline 2018 to 2019. The latter provides the coil currents for the vertical field, whereas the former the reference plasma boundary. A summary of the applied values in this work, together with the resulting plasma shape is given in figure 5.6.

For a quantitative comparison of the shaped NEMEC and ASTRA boundary three parameters are used. The first one is the elongation κ, defined by

$$\kappa = (Z_{max} - Z_{min})/2a \tag{5.4}$$

[1] Measured along the R- and Z-axis independently.

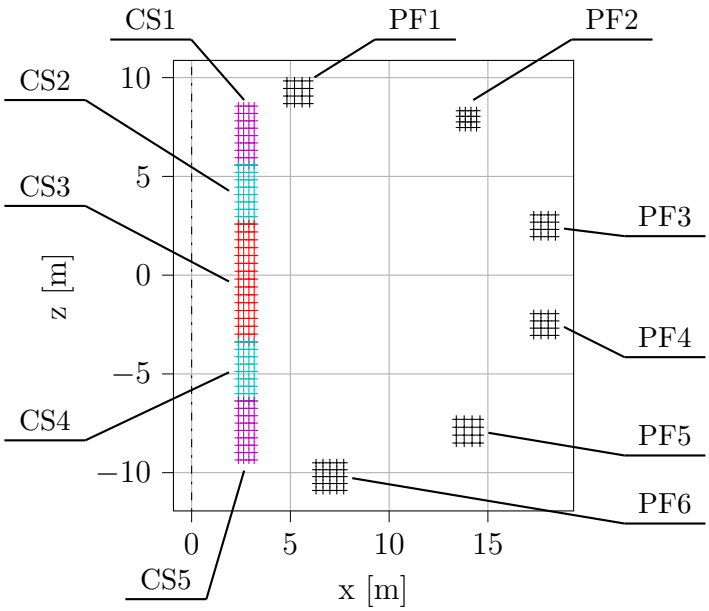

Figure 5.5: Coil filaments for computing a 2D axisymmetric vacuum induction field by MAKEGRID. Each cross indicates the coordinate of a single circular filament in the x-z-plane, which coincides with the plane at $\phi = 0$ in a corresponding toroidal coordinate system. The coordinates are shown in Cartesian coordinates, because this is the applied coordinate system inside MAKEGRID. The rotation around the major axis at $x = 0$ is implicit. For the maximum distance between two neighbouring windings a value of 0.2 m is used in this thesis, because it produces a reasonable filling of the cross section. The central positions of each coil, as well as the width and height are provided by DEMO baseline 2019.

with minor radius a defined as $a = (R_{max} - R_{min})/2$. Z_{max} is the maximum Z-coordinate of the boundary. The quantities Z_{min}, R_{max} and R_{min} are defined analogous. The second and third figure of merit are the upper and lower triangularities δ_{upper} and δ_{lower}, given by

$$\delta_{upper} = (R_{geo} - R_{Z_{max}})/a \tag{5.5a}$$
$$\delta_{lower} = (R_{geo} - R_{Z_{min}})/a \tag{5.5b}$$

with the geometric mean radius $R_{geo} = (R_{max} + R_{min})/2$, the R-coordinate of the boundary point with the maximum Z-coordinate $R_{Z_{max}}$ and $R_{Z_{min}}$ defined analogous to $R_{Z_{max}}$ [29].

To perform the 2D free-boundary NEMEC simulations, an axisymmetric toroidal vacuum induction field is necessary. This field is modeled, by a vertical straight line filament placed at $R = 0$. The coil current is determined by using Stokes theorem for a straight conductor, from which

$$I_{axisym} = \frac{2\pi B_0 R_0}{\mu_0} \tag{5.6}$$

is received, with the on axis toroidal induction field B_0 and the major radius R_0, according to table 4.1 for L-mode and H-mode.

	I^{coil} according to DEMO baseline 2019	applied `extcur`-values		adjusted I^{coil} (n_{cond})	
		L-mode	*H-mode*	*L-mode*	*H-mode*
I_{axisym}	−263.3 MA	1,0	1.0	−263.3 MA (1)	−263.3 MA (1)
PF1	13.3 MA	1.25	1.3	16.6 MA (16)	17.3 MA (16)
PF2	−2.5 MA	1.8	1.9	−4.5 MA (16)	−4.8 MA (16)
PF3	−8.1 MA	0.68	0.79	−5.5 MA (16)	−6.4 MA (16)
PF4	−4.2 MA	0.4	0.43	−1.7 MA (16)	−1.8 MA (16)
PF5	−6.6 MA	1.38	1.45	−9.1 MA (16)	−9.6 MA (16)
PF6	15.8 MA	1.1	1.06	17.4 MA (25)	16.8 MA (25)
CS1	11.9 MA	0.8	0.7	9.5 MA (36)	8.3 MA (36)
CS2	7.8 MA	1.1	1.03	8.6 MA (36)	8.0 MA (36)
CS3	−5.7 MA	1.45	1.15	−8.3 MA (64)	−6.6 MA (64)
CS4	8.0 MA	1.0	1.0	8.0 MA (36)	8.0 MA (36)
CS5	14.7 MA	1.3	1.3	19.1 MA (36)	19.1 MA (36)

(a) Adjustment of coil currents

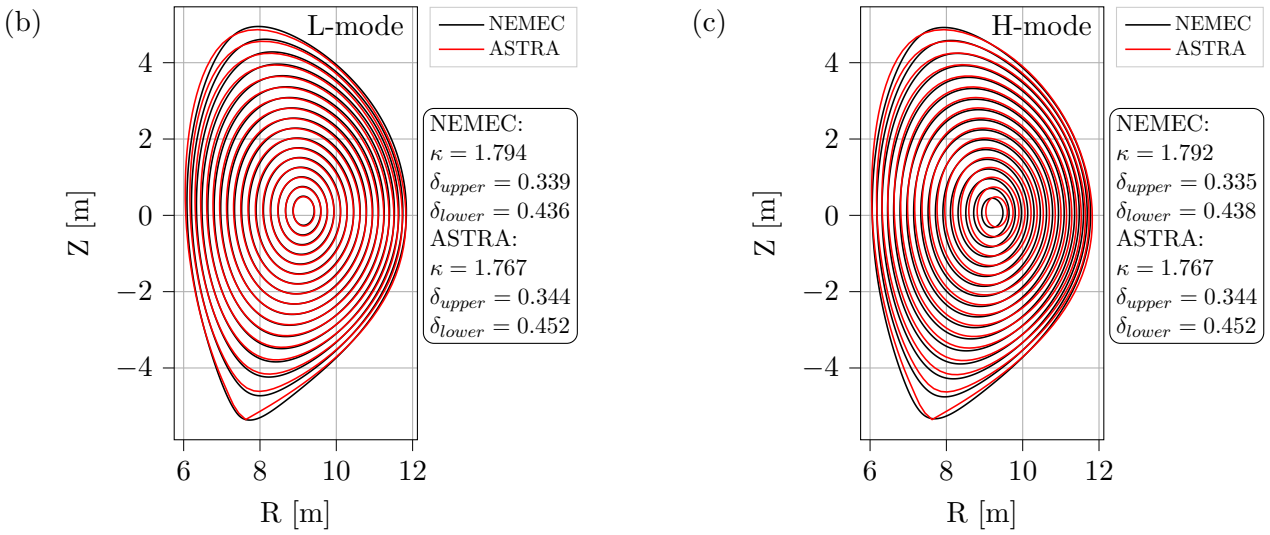

Figure 5.6: (a) Rounded coil current values I^{coil}, flowing through the cross section of the corresponding coil, according to DEMO baseline 2019 for poloidal field coils and central solenoid segments. The coil current I^{coil} is the sum over all currents in the conductors (windings) of the coil, $I^{coil} = \sum I^{cond}$ with I^{cond} of eq. (3.1). I_{axisym} is computed by eq. (5.6) with the engineering values of table 4.1. All coil currents are multiplied with different `extcur`-values for L-mode (b) and H-mode (c) to reproduce the reference boundary of DEMO baseline 2018 (see section 4.1). The adjusted coil currents are given together with the number of conductors n^{cond} for each coil. The comparison of the boundary shape is performed by the elongation κ (eq. (5.4)) and the upper and lower triangularities δ (eq. (5.5)) of the plasma boundary.

5.3.2 3D vacuum induction field. Toroidal field coils

For 3D free-boundary simulations the 2D axisymmetric toroidal field of the previous section needs to be replaced by the vacuum induction field of the toroidal field coils (TF coils). Therefore, the TF coil geometry of figure 4.3 is translated in a comparable manner to the poloidal field coils into MAKEGRID format. The start of the modelling of the TF coils is a set of $\{R, Z\}$-coordinates of a single curve, describing the inner D-shaped circumference. This curve is depicted in figure 5.7 as provided data. The blue TF coil in this figure is created at first and the 15 further TF coils are generated by copying and rotating this coil. Figure 5.7 shows the data in the Cartesian coordinate system used in MAKEGRID. In the following the parametric modelling of this first, blue TF coil is explained, referring to the Cartesian coordinate system. A description based on the coordinates of vectors is used to be closely related to the implementation in MIGEN.

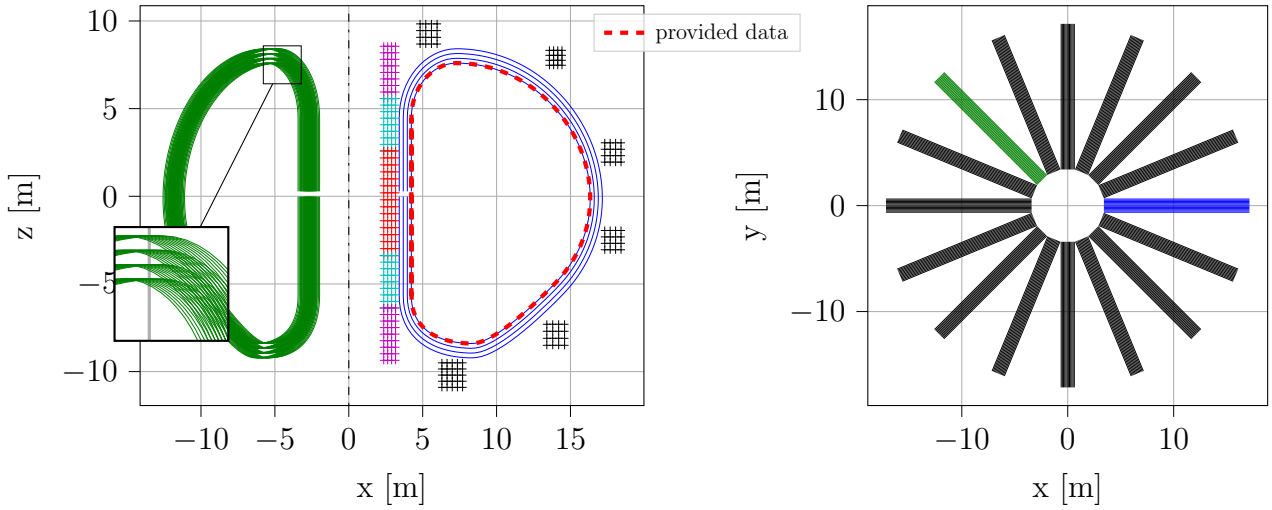

Figure 5.7: Toroidal field coils in front view (left) and top view (right). In the front view the data of figure 5.5 is adopted. The data is shown in Cartesian coordinates, because those are used inside MAKEGRID. In the front view the curve representing the inner circumference of a toroidal field coil is included. This curve is the starting point for the parametric modelling of the coils as described in the text. For the toroidal field coils the maximum spacing between two windings in the x- and y-direction is set by two independent parameters. This is used to align the number of windings in a layer (12) and the number of layers (4) to the cross section of a single toroidal field coil used in [11].

First, a layer of 12 windings with same x- and z-coordinates as the provided data in figure 5.7 is created[2]. This layer can be seen in perspective in the rotated green TF coil. In analogy to the poloidal field coils, this provided data is called the path of the coil. The i-th point of a winding of the first layer is given by

[2]The $\{R, Z\}$-coordinates of the provided do not need to be sorted. A algorithm for sorting these points along the inner circumference is implemented into MIGEN.

$$\begin{aligned} x_i &= x_{i,path} \\ y_i &= -\frac{1}{2}w + j \cdot \Delta y \\ z_i &= z_{i,path} \end{aligned} \tag{5.7}$$

with the width w of the coil in y-direction, j a loop indices running from zero over the number of windings in the first layer $n_{wind,y}$ and the spacing in the y-coordinate between two windings Δy. $n_{wind,y}$ and Δy are computed by the ceil function through

$$n_{wind,y} = \lceil \frac{w}{\Delta y_{max}} \rceil \Rightarrow \Delta y = \frac{w}{n_{wind,y}} \tag{5.8}$$

with a user specified parameter Δy_{max}, determine the maximum spacing between two windings along y-direction.

Second, the cross section is extended into an outward oriented radial direction, viewed from the center of the toroidal field coil. Therefore, in an iterative manner additional layers of windings are added. For the blue TF coil a layer is referred to windings with same x- and z- coordinates, but distinct y-coordinates. These layers can be seen in perspective at the green TF coil in figure 5.7 after a rotation is applied. For the blue coil the first layer is the most inner one, consisting of 12 windings after their the creation according to eq. (5.7). The second layer is created by stretching a copy of the first layer radially outward. For each point in a winding of the first layer a tangential vector is approximated by the difference vector $\vec{d}_{i,j} = \{d_{i,j,x}, d_{i,j,y} = 0, d_{i,j,z}\}$ to the neighbouring point in the same winding, $\vec{d}_{i,j} = \vec{r}_{i+1,j} - \vec{r}_{i,j}$. The subscripts i, j indicate thereby the index of the i-th point in the j-th winding of the first layer. The y component of this difference vector is always 0, because the extrusion is performed in planes parallel to the x-z-plane and hence, represent a 2D problem. These difference vectors are then rotated by 90° around the y-axis, so that they are pointing radially outwards, viewed from the inner of the toroidal field coil. This 90° rotation is performed by

$$\begin{aligned} s_{i,j,x} &= -d_{i,j,z} \\ s_{i,j,y} &= 0 \\ s_{i,j,z} &= d_{i,j,x} \end{aligned} \tag{5.9}$$

with the effectively 2D shift vector of $\vec{s}_{i,j}$ as the resulting vector of the rotation. These shift vectors give the direction into which the i-th point of a copy of the j-th winding of the first layer is displaced to generate the second layer. They are used to generate corresponding points of a winding of the second layer $\vec{r}_{2nd,i,j} = \{x_{2nd,i,j}, y_{2nd,i,j}, z_{2nd,i,j}\}$ by

$$\begin{aligned} x_{2nd,i,j} &= x_{1st,i,j} + \Delta x \cdot \frac{s_{i,j,x}}{|\vec{s}|} \\ y_{2nd,i,j} &= y_{1st,i,j} + \Delta x \cdot \frac{s_{i,j,y}}{|\vec{s}|} \\ z_{2nd,i,j} &= z_{1st,i,j} + \Delta x \cdot \frac{s_{i,j,z}}{|\vec{s}|} \end{aligned} \tag{5.10}$$

based on a copy of the windings of the first layer, indicated with subscript $1st$. Δx is a step width, computed by the number of layers n_{layer} and the thickness t of the TF coil in x-direction, measured at $z = 0$, by

$$n_{layer} = \lceil \frac{t}{\Delta x_{max}} \rceil \Rightarrow \Delta x = \frac{t}{n_{layer}} \tag{5.11}$$

As already mentioned, after the second layer is created the next layer is generated. The second layer takes thereby the role of the first layer and the algorithm is repeated. This iteration continues, until all n_{layer} layers are created.

Besides the geometry of the TF coils, the coil current is needed. The current in all TF coils I_{TF} is equal and is computed by

$$I_{axisym} = 16 \cdot I_{TF} \Rightarrow I_{TF} = \frac{I_{axisym}}{16} \tag{5.12}$$

with the current producing the axisymmetric toroidal vacuum field of eq. (5.6).

5.3.3 Modelling of the ferromagnetic inserts as coils

As introduced in section 4.2 the ferromagnetic inserts are passive elements, composed of ferromagnetic material inside the wall of the vacuum vessel. They interact with the induction field produced by the coil system by aligning existing magnetic moments. These aligned magnetic moments produce a superposing induction field, determined by the geometry of the inserts and the magnetic permeability curve of the material. In [11] the resulting vacuum induction field is computed by using finite element methods. In this work, on the other hand, MAKEGRID is used to compute the vacuum induction field and a coil model for the ferromagnetic inserts has been developed and compared to [11].

In the following the creation of a coil model, reproducing the effect of ferromagnetic inserts (FIs) is explained for one ferromagnetic insert (FI). All further 15 FI volumes are treated equally. The FIs are considered to be in a static state. Hence, no currents are present. The quantitative description starts by dividing the volume of the FI into five segments in the poloidal direction. For each segment a representative magnetic moment $\vec{m}_{FI}$ is computed. This magnetic moment emerge, because the existing microscopic magnetic moments in the ferromagnetic material align with the field of the toroidal field coils they are exposed to. For the computation of $\vec{m}_{FI}$ a segment is split into smaller regions in the poloidal cross section and a local magnetic moment $\vec{m}_{local}$ for each of these regions is computed. Both magnetic moments are visualized in figure 5.8. All magnetic moments $\vec{m}_{FI}$ produce a magnetic dipole field, increasing the field strength inside the FI, but weaken it outside of the FI, where the plasma boundary is. Thus, the regions underneath the toroidal field coils with higher magnetic induction are reduced at the plasma boundary and subsequently the toroidal field ripple decreases.

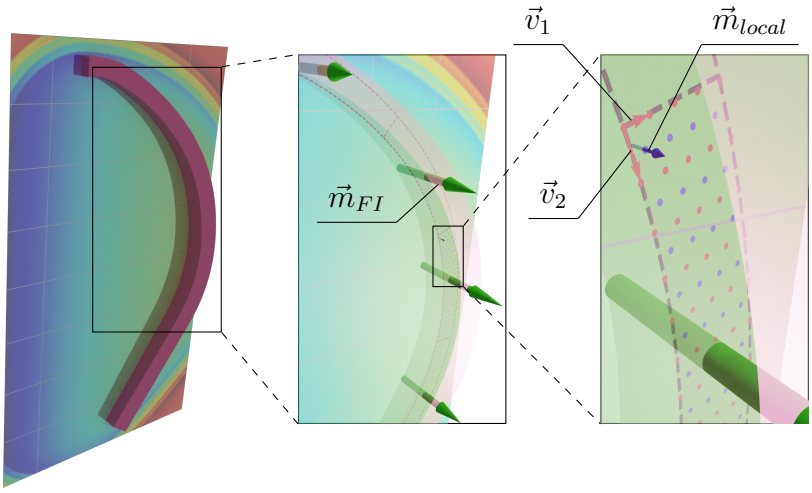

Figure 5.8: Ferromagnetic insert (magenta volume) in exposed magnetic induction field generated by toroidal field coils. The exposed toroidal vacuum field is visualized by a color plot on the center plane of a ferromagnetic insert. Jumps of the field strength can be seen around the ferromagnetic insert, where the toroidal field coils are located. A ferromagnetic insert is split into several segments and for each segment a representative magnetic moment $\vec{m}_{FI}$ is computed. In this work ferromagnetic inserts are divided into five segments. $\vec{m}_{FI}$ is the vector sum of several local magnetic moments $\vec{m}_{local}$. For every blue point inside a segment $\vec{m}_{local}$ is computed according to eq. (5.13), where R_{local} is the radius of the position of the corresponding $\vec{m}_{local}$-vector related to the major axis of the torus and $A_{local} = |\vec{v}_1 \times \vec{v}_2|$ is the area spanned by the local vectors $\vec{v}_1$ and $\vec{v}_2$.

The toroidal component $m_{FI,\phi}$, which is relevant for the investigation of the toroidal field ripple, is computed by

$$m_{FI,\phi} = \sum m_{local,\phi} \tag{5.13a}$$
$$= \sum M_\phi \cdot V_{local} \tag{5.13b}$$
$$= \sum M_\phi \cdot A_{local} \cdot R_{local} \cdot \Delta\phi \cdot ff \tag{5.13c}$$

with summation over all blue points of the corresponding FI segment, depicted for outboard midplane in figure 5.8. The mean magnetization per volume M_ϕ is extracted from the magnetic permeability curve based on the exposed vacuum field at the location of $\vec{m}_{local}$ (blue points) by eq. (5.14). M_ϕ is multiplied by a local volume V_{local}. This local volume is spanned by a small area in the poloidal cross section, A_{local}, extruded along a curve with fixed radius R_{local} and rotation around the major axis of the torus of $\Delta\phi$. A_{local} is spanned by the vectors $\vec{v}_1$ and $\vec{v}_2$, depicted in figure 5.8. $\Delta\phi$ is a parameter, for which the value $\Delta\phi = 6.5°$ is used, as in [11]. Furthermore a filling factor ff with values $[0, 1]$, giving the amount of ferromagnetic material inside the volume of the ferromagnetic inserts, is applied as parameter. This filling factor is also included in the investigations of [11], because the FI can overcompensate the toroidal field ripple. Therefore it is necessary to reduce the amount of ferromagnetic material in the FI volume, in order to minimize the toroidal field ripple.

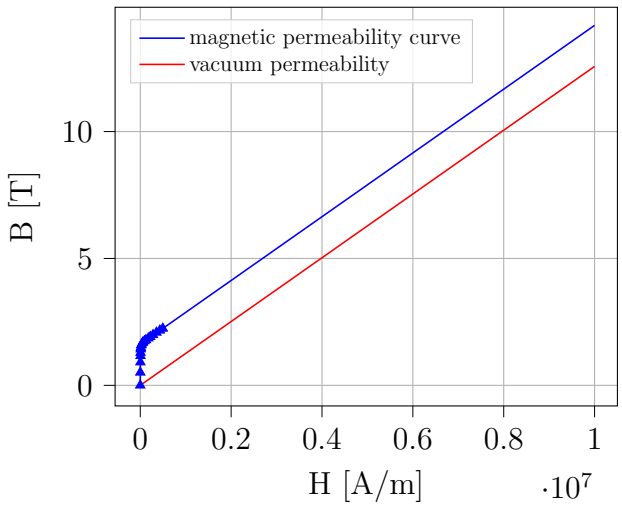

Figure 5.9: Magnetic permeability curve used to compute the magnetization of the ferromagnetic inserts. The marked data points are given in [11]. The extrapolation for the saturated region is based on the vacuum permeability.

The magnetization of the material M_ϕ is extracted from the magnetic permeability curve[3]. Therefore, the vacuum induction field of the toroidal field coils $B_{vac,\phi} = B_{exposed,\phi}$ is interpreted as field to which the ferromagnetic inserts are exposed to. This induction field is translated to a vacuum magnetic field $H_{exposed,\phi} = B_{exposed,\phi}/\mu_0$. The value of $H_{exposed,\phi}$ is used to read out the value of the induction field inside the ferromagnetic insert $B_{FI,\phi}$ according to the magnetic permeability curve, shown in figure 5.9. The induction field inside the ferromagnetic inserts consists of $B_{FI,\phi} = \mu_0(H_{exposed,\phi} + M_\phi)$ and thus the magnetization is given by

$$M_\phi = \frac{1}{\mu_0}(B_{FI,\phi} - B_{exposed,\phi}) \tag{5.14}$$

with $B_{exposed,\phi} = \mu_0 H_{exposed,\phi}$.

To reproduce the magnetic moments $m_{FI,\phi}$ in MAKEGRID, windings of current carrying filaments are wrapped around each segment, so that they produce a magnetic moment aligned to $\vec{m}_{FI}$ in figure 5.8. The applied geometry of the windings of these FI coils is shown in figure 5.10. Inside MIGEN the FI coils are generated similar to the toroidal field coils, explained in detail in section 5.3.2. First a curve as the provided data in figure 5.7 is split into a user specified number of segments. This curve describes a section of the inner poloidal contour of the vacuum vessel. Next, for each segment the first winding is closed around the segment. Therefore, the inner contour is copied and shifted by shift vectors as in eq. (5.10) radially outward by the thickness of the wall of the vacuum vessel. This first winding is subsequently copied and rotated around the major axis of the torus, to generate all windings of a segment over the toroidal spacing of a FI of $\Delta\phi = 6.5°$.

In addition to the geometry, the coil currents of the FI coils need to be computed. Therefore the magnetic vacuum induction field is written as $\vec{B}_{vac} = \vec{\nabla} \times \vec{A}_{vac}$ with the corresponding vector potential $\vec{A}_{vac}$. For a given current density $\vec{j}(\vec{r})$ the vector potential is

[3]The subscript ϕ in M_ϕ indicates, that for the external field solely the contribution of the toroidal field coils is used.

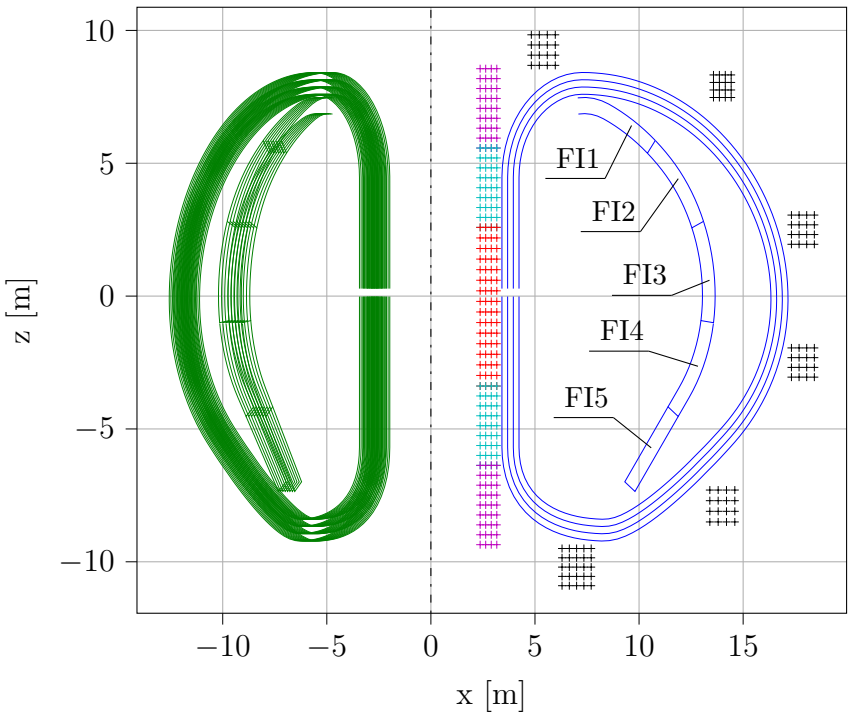

Figure 5.10: Geometry of the ferromagnetic inserts coil model (FI coil) in MAKEGRID format. A single ferromagnetic insert is divided into five segments with eight windings around a segment, labeled with FI1 to FI5 for one example. A increase in the number of windings and segments showed no substantial effect in the simulations within this thesis. Five FI coils are located underneath each toroidal field coil. For transparency only two toroidal field coils with FI coils are depicted. The coil system of figure 5.5 and 5.7 is adopted for completeness in this plot. The poloidal shape of the FI coils is chosen to span the thickness of the vacuum vessel wall along the circumference over a region with optimal reduction of the toroidal field ripple, according to [11]. This region of the ferromagnetic inserts is referenced as case02 in [11].

$$\vec{A}(\vec{r}) = \frac{\mu_0}{4\pi} \int d^3r' \frac{\vec{j}(\vec{r'})}{|\vec{r} - \vec{r'}|} \tag{5.15}$$

This can be expanded by using the multipole expansion

$$\frac{1}{|\vec{r} - \vec{r'}|} = \frac{1}{r} + \frac{\vec{r'} \cdot \vec{r}}{r^3} + ...$$

The first term is describing a monopole, which vanishes for magnetic fields. Starting with the first, non vanishing term one can express the vector potential of the vacuum field as

$$\vec{A}(\vec{r}) = \frac{\mu_0}{4\pi} \frac{\vec{m} \times \vec{r}}{r^3} + ... \tag{5.16}$$

with the magnetic dipole moment $\vec{m}$, defined in (5.16) as [30]

$$\vec{m} = \frac{1}{2} \int \vec{r'} \times \vec{j}(\vec{r'}) d^3r' \tag{5.17}$$

Now the magnetic moment is expressed in terms of the coil current I, which is the same in all filaments (windings), instead of the current density $\vec{j}$. Therefore, the transition between a spatially distributed current density $\vec{j}$ and the i-th filament l_i, carrying the current I, is done by using the substitution $\vec{j} d^3r \rightarrow I d\vec{l_i}$ [30]. This gives

$$\vec{m}_{coil} = \frac{I}{2} \sum_i \int \vec{r} \times d\vec{l_i} \tag{5.18}$$

with the differential vector $d\vec{l_i}$ along the i-th filament. The sum includes all filaments of the FI coil in figure 5.10.

For the FI coil to reproduce $m_{FI,\phi}$, the ϕ component of $\vec{m}_{coil}$ is forced to be the equal to eq. (5.13): $m_{coil,\phi} \stackrel{!}{=} m_{FI,\phi}$. This gives the relation for the coil current

$$I = \frac{2 m_{FI,\phi}}{\left(\sum_i \int \vec{r} \times d\vec{l_i} \right)_\phi} \tag{5.19}$$

The integral in the denominator is computed numerically. For the numerical computation of the integral, it is used, that this integral is independent of the choice of the origin of $\vec{r}$, because it is determined by the poloidal cross section area $F = \sum A_{local}$ of the FI coil, which is invariant under spatial transformations [30].

$$\begin{aligned} \int_{\partial F} \vec{r} \times d\vec{l} &= - \int_F (d\vec{f} \times \vec{\nabla}) \times \vec{r} \\ &= \int_F (\vec{\nabla} \cdot \vec{r}) \cdot d\vec{f} - \vec{\nabla} \cdot (\vec{r} \cdot d\vec{f}) \\ &= \int_F 2 d\vec{f} \\ &= 2F \end{aligned} \tag{5.20}$$

In line two it is used, that $\vec{r}$ can be chosen in a plane with $d\vec{l}$. Then $\vec{r} \cdot d\vec{f} = 0$ and for the case of a plane $\vec{\nabla} \cdot \vec{r} = 2$. Afterwards the result can be transformed into other coordinate systems. However, this leaves the cross section area F unchanged.

Comparison to report [11].

In [11] the toroidal field ripple $\tilde{\delta}$ (eq.(2.13)) is computed for a 3D vacuum induction field of DEMO baseline 2017, using finite element methods. Thereby a parametric study on the filling factor ff of eq. (5.13) is carried out. A value of $ff = 0$ is equivalent to section 5.3.2, where no ferromagnetic inserts are contained. The total volume of ferromagnetic inserts in figure 4.3 filled with material corresponds to a value of $ff = 1$. In figure 5.11 a comparison between the computations in [11] and the presented FI coil model in MAKEGRID is presented. This comparison shows, that the FI coil model describes qualitatively the same behaviour of FIs

as in [11]. Increasing the filling factor from 0 to 1, the toroidal field ripple first decreases. At a optimal filing factor the FIs begin to overcompensate and hence, increase the toroidal field ripple again. The overcompensation starts at outboard midplane, because the volume of the FIs in this region is the largest.

The parametric scan of the filling factor shows, that the FI coil model can reproduce $\tilde{\delta}_{sep}$[4] of [11] also quantitatively, until a filling factor of 0.4. Increasing the filling factor further leads to deviations, because the overcompensation at outboard midplane is described weaker in the FI coils than in [11]. In [11] a optimal filling factor is found at $ff = 0.4$. For this value the FI coils and [11] show consistent values and therefore the 3D vacuum field belonging to $ff = 0.4$ is used in all results of this thesis.

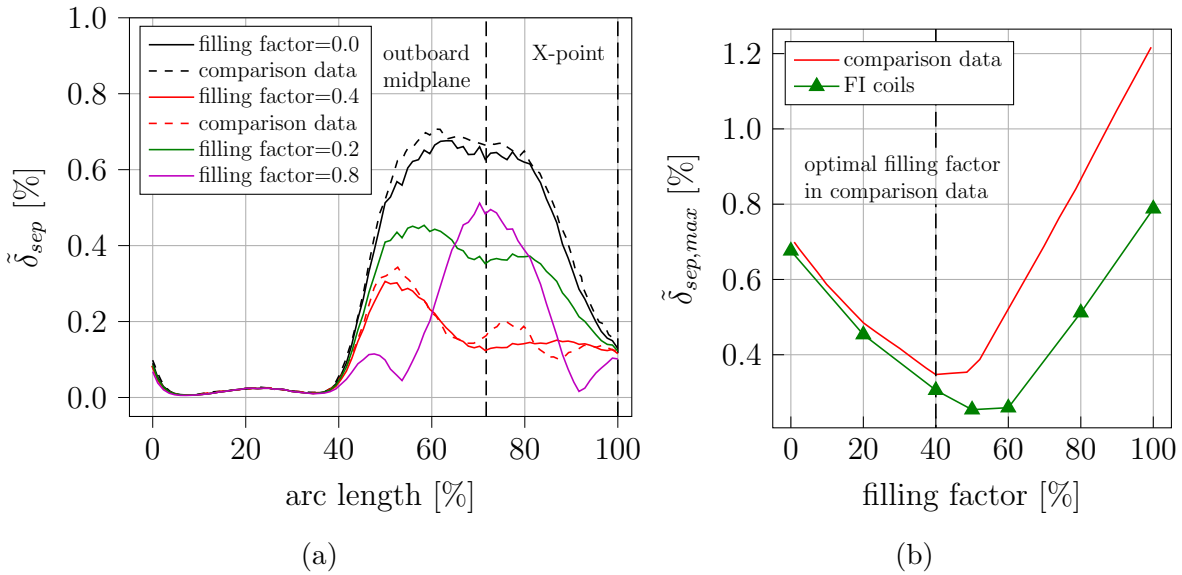

(a) (b)

Figure 5.11: Comparison of the coil model for ferromagnetic inserts (FI coils) to the data of the report in [11], marked here as comparison data. In the report the toroidal field ripple in the vacuum $\tilde{\delta}_{sep}$ (eq. (2.13)) is computed on the separatrix of DEMO baseline 2017. The therefore needed vacuum induction field, produced by toroidal field coils with ferromagnetic inserts, is in [11] computed by a finite element approach. (a) shows $\tilde{\delta}_{sep}$ as a function of the the arc length of the separatrix. For the FI coil data to be comparable to [11], the $\tilde{\delta}_{sep}$ curves are also related to the DEMO baseline 2017 separatrix. Several curves for different filling factors (see eq. (5.13)) are included. In (b) a parametric scan of the filling factor is shown, where for different filling factors $\tilde{\delta}_{sep,max}$ is computed by $\tilde{\delta}_{sep,max} = \max[\tilde{\delta}_{sep}(\text{arc length})]$ with $\tilde{\delta}_{sep}$ for the corresponding filling factor. In [11] it is stated, that a optimal reduction of the toroidal field ripple is achieved for a value of 40 %, as marked in this plot. The report is based on DEMO baseline 2017 scenario, with $B_0 = 4.89\,\text{T}$ and $R_0 = 8.938\,\text{m}$. Therefore, MIGEN is used to create MAKEGRID input with the same toroidal field for this comparison. The number of windings in a toroidal field coil is adjusted to this report all over this work.

[4] $\tilde{\delta}_{sep} = \tilde{\delta}$ on the DEMO baseline 2017 separatrix.

Potential causes for the deviation of FI coils and [11] in figure 5.11 are:

- The computation of the FI coil current according to eq. (5.19) is sensitive to the underlying magnetic permeability curve. The curve used in this thesis is extrapolated with vacuum permeability, because of missing data points, as shown in figure 5.9. The exposed vacuum induction field $B_{exposed,\phi}$ in eq. (5.14) takes absolute values in the extrapolated region. It is not clear, if the extrapolation is performed in the same way.
- The filling factor ff in eq. (5.13) is assumed to be uniformly distributed in the radial and toroidal direction. This is so far an assumption based on the available information and needs to be verified.

The modeling of the geometry of the FI coils is not considered as a potential cause of the deviations. The reason for this is the manual adjustment of the FI coil currents in figure 5.12, showing that the FI coil geometry is able to reproduce the data from [11] over the whole range of the filling factor. However, this adjustment of the coil currents has no physical basis so far.

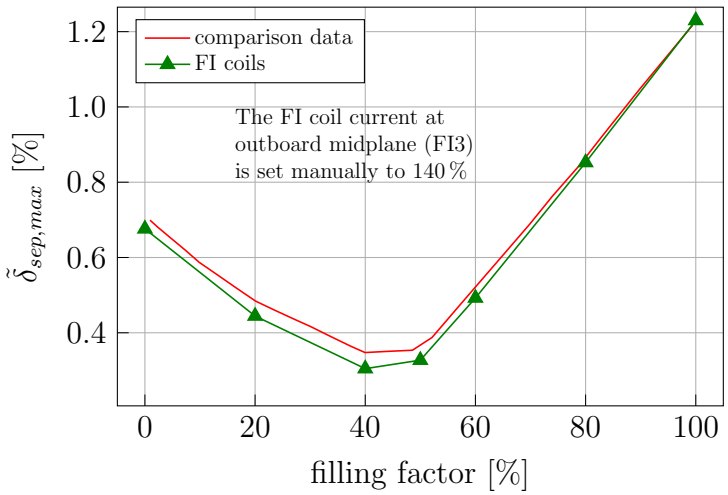

Figure 5.12: Manual adjustment of the FI coil currents to show, that the geometry of the FI coils is able to reproduce the data of [11], marked here as comparison data. As in figure 5.11, $\tilde{\delta}_{sep,max} = \max[\tilde{\delta}_{sep}(\text{arc length})]$, with $\tilde{\delta}_{sep}(\text{arc length})$ computed over the arc length of the DEMO baseline 2017-separatrix, for the corresponding filling factor (eq. (5.13)). The difference to figure 5.11 (b) in this plot is, that the coil current of FI3, located at outboard mid plane (see figure 5.10), is manually set to 140 % of the value according to eq. (5.19). The other FI coil currents are unchanged to eq. (5.19). This adjustment has no physical basis, but shows that the geometry of the FI coils can reproduce the data of [11]. As for figure 5.11, the data of [11] and the FI coils is based on DEMO baseline 2017 with $B_0 = 4.89\,\text{T}$ and $R_0 = 8.938\,\text{m}$.

6 Plasma response to the toroidal field ripple

6.1 L-mode

6.1.1 Corrugation of flux surfaces

In section 5.1 a general workflow is described to perform 3D free-boundary simulations in NEMEC, starting from ASTRA output. The required 3D vacuum field for these simulations is based on a realistic model of 16 toroidal field coils. Due the toroidal spacing between these toroidal field coils, the toroidal field ripple is present in the vacuum field, as investigated at the end of section 5.3.3. By results of 3D free-boundary NEMEC simulations the corrugation of flux surfaces, as plasma response to the toroidal field ripple, is presented in this section. The key figure to quantify the flux surface corrugation applied in this section is the amplitude of the corrugation $\delta(R, Z)$, computed according to eq. (2.14). $\delta(R, Z)$ is shown in figure 6.1 for vacuum fields with and without ferromagnetic inserts.

The plasma response is expected to have a 16-fold symmetry in the toroidal direction, because of the 16 equally spaced toroidal field coils around the major axis of the torus. This is used to reduce the computational load, by specifying in NEMEC a number of field periods $N_p = 16$. Hence, NEMEC computes the flux surface only on a section of the toroidal circumference of $2\pi/16$. This section is then repeated 16 times in the toroidal direction to reconstruct the complete torus. The Fourier series of eq. (3.13) can be rewritten, to show the N_p parameter explicitly as

$$R = \sum_{m,n} \left[\hat{r}^c_{m,n}(s) \cdot \cos(m\theta - n \cdot N_p\zeta) + \hat{r}^s_{m,n}(s) \cdot \sin(m\theta - n \cdot N_p\zeta) \right] \tag{6.1a}$$

$$Z = \sum_{m,n} \left[\hat{z}^c_{m,n}(s) \cdot \cos(m\theta - n \cdot N_p\zeta) + \hat{z}^s_{m,n}(s) \cdot \sin(m\theta - n \cdot N_p\zeta) \right] \tag{6.1b}$$

with the Fourier components $\hat{r}^c_{m,n}, \hat{r}^s_{m,n}, \hat{z}^c_{m,n}, \hat{z}^s_{m,n}$, magnetic coordinates s, θ, ζ and poloidal and toroidal mode number m, n [31]. In the NEMEC simulations of this thesis the values $n = 0$ and $n = 1$ of eq. (6.1) are included. This has the consequence, that only effects according to values of the toroidal mode number $n \cdot N_p = 0$ and $n \cdot N_p = 16$, related to complete toroidal circumference of 2π, can be observed in the data of this section.

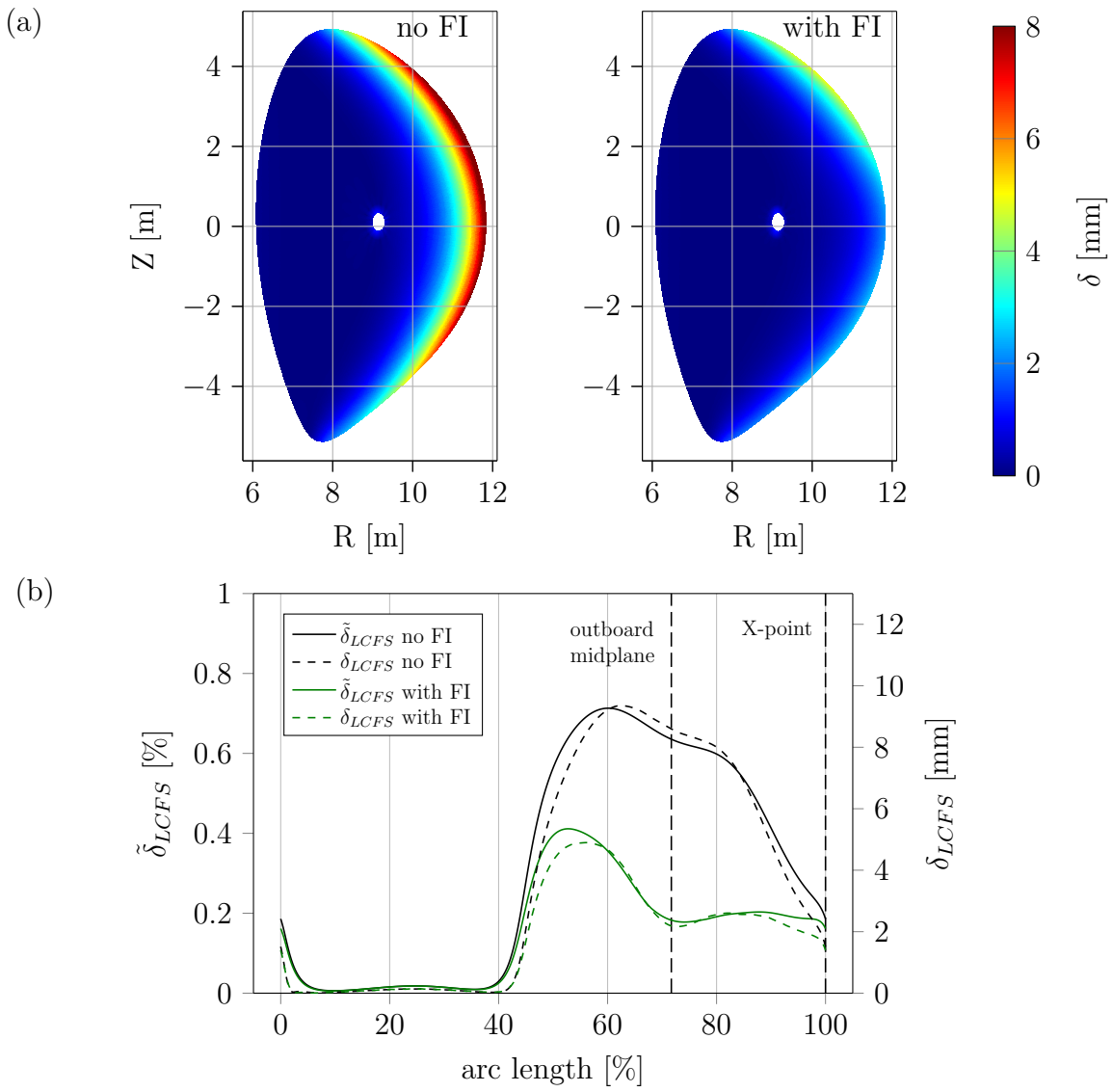

Figure 6.1: (a) shows the amplitude of the flux surface corrugation $\delta(R, Z)$, according to eq. (2.14) in a poloidal cross section. The 3D flux surfaces, for the computation of $\delta(R, Z)$, are a result of 3D free-boundary NEMEC simulations for a vacuum field without ferromagnetic inserts (left) and with ferromagnetic inserts (right). To resolve the corrugation a NEMEC-grid consisting of 16 toroidal equally spaced planes and 300 points in the θ coordinate are used. The 16-fold periodicity is used, to specify the number of field periods $N_p = 16$, see text. Further numerical parameters are the subject of the convergence study below.
(b) shows the toroidal field ripple of the vacuum $\tilde{\delta}(R, Z)$, according to eq. (2.13), in comparison to $\delta(R, Z)$ for $\{R, Z\}$-coordinates on a axisymmetric LCFS. This axisymmetric LCFS is reconstructed from 3D NEMEC simulations, using eq. (6.1) with $n = 0$.
Data in (a) and (b) is based on the engineering parameters of table 4.1 and the coil system described in section 4.2. Vacuum fields with ferromagnetic inserts (FI) refer to a filling factor of 0.4 in section 5.3.3.

Figure 6.1 shows, that the highest values for the amplitude of the flux surface corrugation $\delta(R, Z)$ without ferromagnetic inserts are observed at the outboard position on the low field side of the toroidal field. The amplitude of the corrugation decreases towards the magnetic axis. At the high field side of the toroidal field, on the inner side of the torus, $\delta(R, Z)$ is negligible. This is consistent with expectations, because toroidal field coils have no spacing between each other at the circumference of the central solenoid, but the space increases towards the low field side as illustrated in figure 1.4. Furthermore, figure 6.1 contains a comparison between the toroidal field ripple in the vacuum field $\tilde{\delta}$ and the plasma response δ, for the cases with and without ferromagnetic inserts. It is observed, that the reduction of the toroidal field ripple on the LCFS translates directly into the amplitude of the flux surface corrugation. With and without ferromagnetic inserts the toroidal field ripple and the amplitude of the flux surface corrugation are distributed equally over the low field side. Additionally, the highest value of $\tilde{\delta}$ and δ, with inclusion of ferromagnetic inserts, is in the same region of the LCFS. The maximum value along the LCFS of $\tilde{\delta}_{LCFS}$ is reduced from 0.71 % to 0.41 %. This decrease by 42 % translates into δ_{LCFS}, which is reduced by 48 % in the maximum value. This observation is consistent with the expectation, that the toroidal field ripple is a non-resonant perturbation, as explained in section 2.3. A further confirmation of this conclusion can be seen in the numerical convergence of $\delta(R, Z)$, shown in figure 6.2. By keeping the force tolerance below a threshold for reasonable results one can see, that a small number of radial grid points is sufficient to resolve the flux surface corrugation.

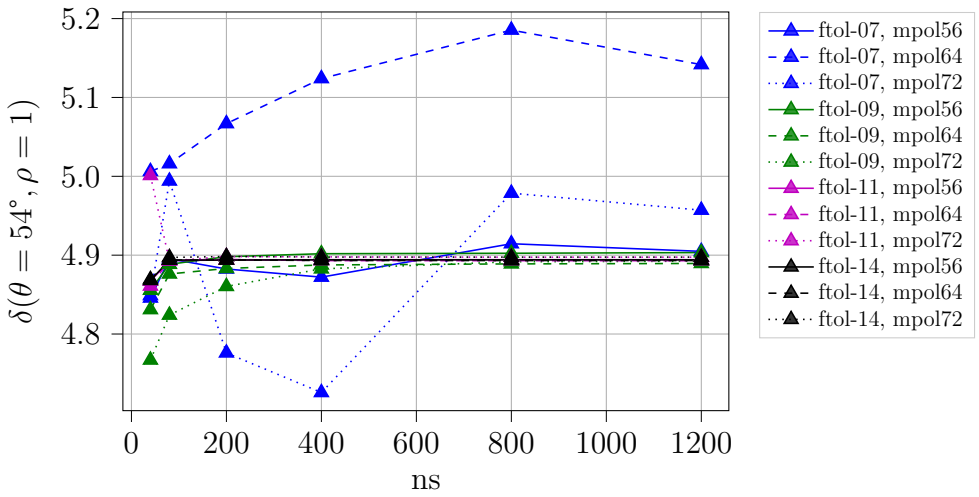

Figure 6.2: Numerical convergence of δ (eq. (2.14)) at a position of $\theta = 54°$ on the plasma boundary for a vacuum field including ferromagnetic inserts. The parameters are the number of radial grid points `ns`, the force tolerance level `ftol` and the number of poloidal harmonics `mpol` (see section 3.4). It is shown, that a converged value of the flux surface corrugation can be assumed, with 800 radial grid points and a force tolerance level of $1 \cdot 10^{-11}$. Same plots for different poloidal angles θ confirm this conclusion. All presented results in this section are computed with these two values, together with a poloidal mode number `mpol` of 72, which is the highest value achieved in NEMEC simulations in this work.

6.1.2 Comparison to vacuum approximation

In this section the plasma response δ computed by 3D NEMEC simulations of the previous section is compared to the so-called vacuum approximation. The vacuum approximation is an independent superposition of two contributions to this magnetic field :

1. An axisymmetric induction field $\vec{B}_{2D}$ of a 2D MHD equilibrium.
2. The toroidal field ripple in the vacuum induction field $\vec{B}_{ripple}$.

First, the MHD equilibrium is computed by a 2D free-boundary NEMEC simulation. To obtain $\vec{B}_{2D}$ for this equilibrium on the same grid as in MAKEGRID, the BMW code (**B**iot-Savart **M**agnetic **V**MEC **V**ector potential) is used [12]. The computation on the same grid simplifies the superposition with $\vec{B}_{ripple}$, computed by MAKEGRID. BMW uses the plasma current density $\vec{j}_{pl}$ computed by NEMEC and the corresponding vacuum field, which is applied in the NEMEC simulation, computed by MAKEGRID for the reconstruction. MAKEGRID contains besides the vacuum induction field for the free-boundary simulation also the related vector potential $\vec{A}_{vac}$. With these two quantities BMW reconstructs the magnetic induction field $\vec{B}_{2D}$ inside and outside the plasma by [12]

$$\vec{A}_{2D}(\vec{r}) = \frac{\mu_0}{4\pi} \int_{\Omega_{pl}} \frac{\vec{j}_{pl}(\vec{r'})}{|\vec{r} - \vec{r'}|} d^3r' + \vec{A}_{vac}(\vec{r}) \tag{6.2a}$$

$$\vec{B}_{2D}(\vec{r}) = \vec{\nabla} \times \vec{A}_{2D}(\vec{r}) \tag{6.2b}$$

For the second contribution, $\vec{B}_{ripple}$, the 3D vacuum induction field produced by the coils in figure 5.7 is modified in a way, that the toroidal field ripple is extracted. For this extraction a straight filament on the z-axis at $x = y = 0$ in the coil system of figure 5.7 is added. This straight filament is identical to the one which produced the 2D axisymmetric toroidal field in section 5.3.1, but now the current is flowing in the reversed direction. In the 3D coil system of figure 5.7 the contribution of this reversed current in the central straight filament on the z-axis suppresses the axisymmetric contribution of the toroidal field and thus, the toroidal field ripple $\vec{B}_{ripple}$ is extracted. The necessity for this central straight filament can be seen by recognizing, that without it the axisymmetric contribution to the toroidal field would be accounted twice. One time in $\vec{B}_{2D}$ in the vacuum field of the 2D free-boundary NEMEC simulation and again in the superimposed 3D field from the toroidal field coils.

The vacuum approximation is a superposition of magnetic fields, without giving us directly the coordinates of the resulting flux surfaces. To compute a corrugation amplitude δ in eq. (2.14) for the vacuum approximation, the connection length of field lines is computed. The connection length of a field line is the spatial length of a curve, following the magnetic field. The connection length is computed iteratively, following the field lines. It ends, if the coordinates of the curve leave the computational grid, surrounding the plasma, or after a fixed number of iterations. Thus, a sharp transition between confined (higher connection length) and unconfined (smaller connection length) field lines is expected, because the confined field lines circulate infinitely around the torus. This is shown in figure 6.3 for a coil system without ferromagnetic inserts. A comparison to the inherent 3D NEMEC simulations is added, by

using again BMW for a reconstruction of the magnetic field. This 3D data is not created as superposition, because the toroidal field ripple is already contained in eq. (6.2) of BMW.

Figure 6.3 shows that the transition between confined and unconfined field lines does not coincident with the LCFS of NEMEC simulations. Besides numerical inaccuracies, this can be explained by the observation, that the transition of low to high connection length is described by the separatrix, which can not be resolved in NEMEC due to the finite number of poloidal harmonics. To ease then the comparison, two lines of constant connection length are depicted in figure 6.3, one at the transition and one on the opposite of the LCFS. For both lines the corrugation amplitude δ shows differences between vacuum approximation and 3D NEMEC simulation of 2.3 mm and 1.4 mm. This is a deviation of the vacuum approximation between 26 % and 17 % to the 3D NEMEC simulation. Hence, the vacuum approximation can not fully capture the plasma response to the toroidal field ripple.

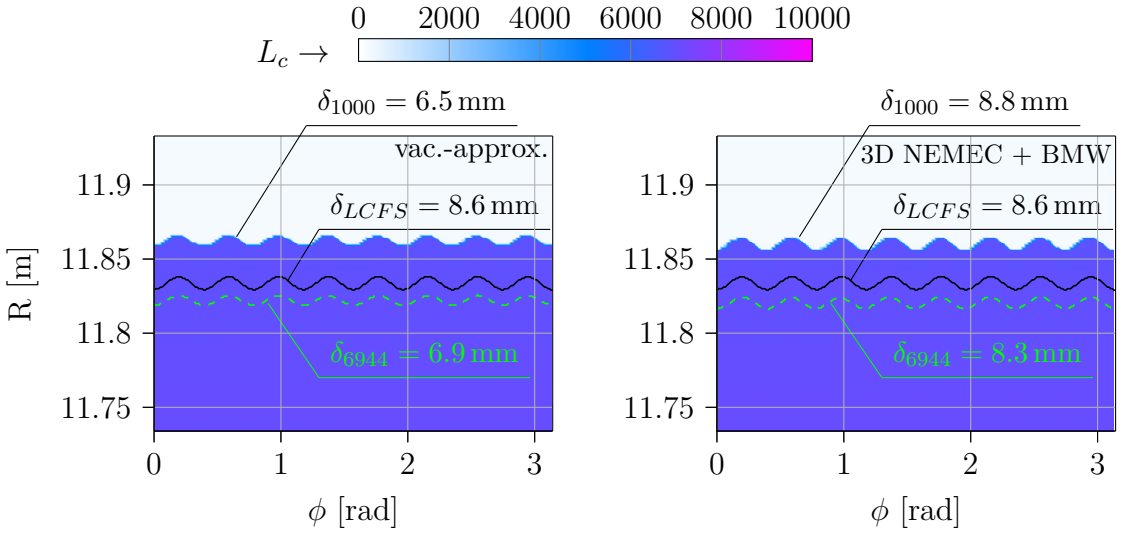

Figure 6.3: Comparison of connection length L_c of field lines in the vacuum approximation (left) and of 3D NEMEC simulation (right) in the outboard mid plane at $Z = Z_{axis}$. In both cases the magnetic field lines are reconstructed using BMW, as explained in the text. A transition from confined (high L_c) to unconfined (low L_c) field lines is marked with a line of a constant value of the connection length of $L_c = 1000\,\text{m}$. Furthermore a second line of constant connection length with $L_c = 6944\,\text{m}$ is marked, because the transition between confined and unconfined field lines is located at a bigger radius R than the LCFS of the 3D NEMEC simulation. For all marked lines, the amplitude of the corrugation is given by $\delta = \max[R(\phi)] - \min[R(\phi)]$. NEMEC simulations for this plot (2D free-boundary for vacuum approximation, as well as the 3D free-boundary) are computed with 800 radial grid points and a force tolerance level of $1 \cdot 10^{-11}$, which are the converged values according to section 6.1.1.

6.2 Comparison between L-mode and H-mode

The comparison between the L-mode and the H-mode in this section is performed in terms of the amplitude of the flux surface corrugation δ (eq. (2.14)), computed based on flux surfaces from 3D free-boundary NEMEC simulations. The vacuum induction field for these simulations is the same as used in section 6.1.1, where exclusively the plasma response of the L-mode is presented. This vacuum induction field is computed by MAKEGRID based on the engineering parameters in table 4.1 and the coil system shown in section 4.2. In the data of this section only effects related to the toroidal mode numbers 0 and 16 can be observed. The reason for this is the same as for the L-mode and is explained in section 6.1.1 based on eq. (6.1).

In figure 6.4 $\delta(R, Z)$ is shown for H-mode and L-mode in a poloidal cross section, for a vacuum induction field containing ferromagnetic inserts for the reduction of the toroidal field ripple. It is observed, that the absolute values of $\delta(R, Z)$ show no significant difference between H-mode and L-mode. Furthermore, the color plot, decoding the amplitude $\delta(R, Z)$, shows for both plasma scenarios the maximum ripple above outboard mid plane in the plasma edge and a smaller, but non-zero, value in the plasma edge below outboard mid plane. This is expected, based on the conclusion in section 6.1.1, that the plasma shows no interaction with the toroidal field ripple in the vacuum field.

The numerical parameters for the H-mode and the L-mode in figure 6.4 are the same as in section 6.1.1. Thereby a fluctuation in $\delta(R, Z)$ for the H-mode in the plasma edge can be observed, which is not present in L-mode. For the visualization of the fluctuation δ is plotted along the highlighted θ-lines. There it can be seen, that the fluctuation is located in the plasma edge between a rational flux surface with $q = 3$ and the LCFS, solely for H-mode in a vacuum induction field with ferromagnetic inserts. However, this fluctuation vanishes if the force tolerance `ftol` is lowered and NEMEC consequently computes flux surfaces with smaller residual forces for the equilibrium, as depicted in figure 6.5. Therefore the fluctuation is not an indicator for a resonant perturbation.

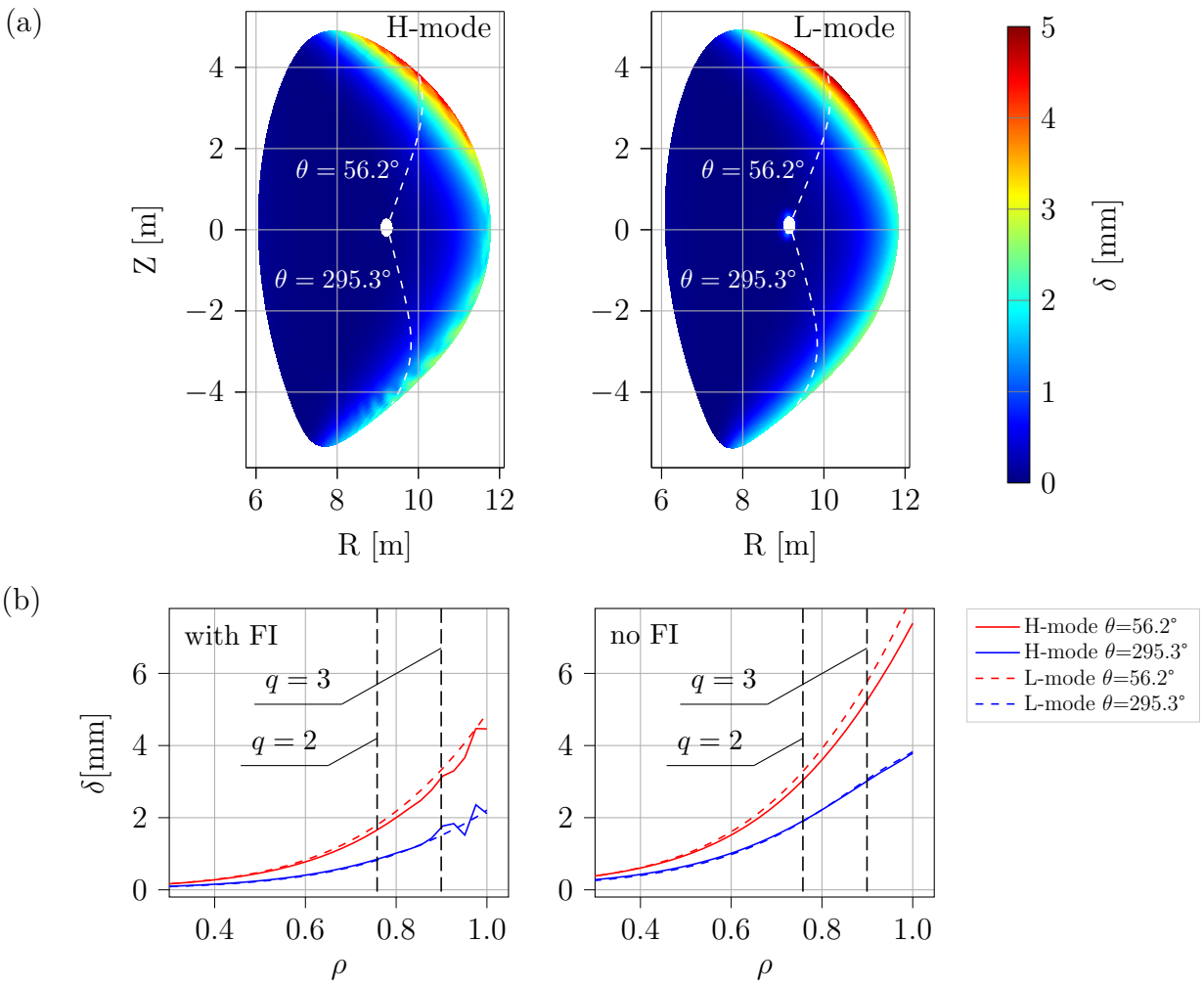

Figure 6.4: (a) shows a poloidal cross section containing a color plot for $\delta(R, Z)$, according to eq. (2.14). The 3D flux surfaces for the computation are results of 3D free-boundary NEMEC simulations with a vacuum induction field with ferromagnetic inserts for the ripple reduction. On the left side the H-mode from section 4.1.2 is shown and on the right side the L-mode from section 4.1.1. In both simulations a value for the number of field periods $N_p = 16$, in combination with a maximum toroidal mode number $n = 1$, is used (see section 6.1.1). The grid inside NEMEC uses `ns`=800, 300 points in the poloidal plane for a flux surface and 16 planes in the toroidal direction. Further numerical parameters are the force tolerance `ftol`=$1 \cdot 10^{-11}$ and the maximum number of poloidal harmonics `mpol`=72. These values are chosen based on the convergence study of the L-mode in figure 6.2. All numerical parameters are identical for H-mode and L-mode in this plot.
(b) shows $\delta(R, Z)$ along the θ-lines highlighted in (a) for vacuum induction field with and without ferromagnetic inserts (FI). The position of rational flux surfaces with $q = 2$ and $q = 3$ is marked. The fluctuation for the H-mode with ferromagnetic inserts vanishes, if the force tolerance `ftol` is lowered, see figure 6.5.
Data in (a) and (b) is based on the engineering parameters of table 4.1 and the coil system described in section 4.2. Vacuum fields with ferromagnetic inserts (FI) refer to a filling factor of 0.4 in section 5.3.3.

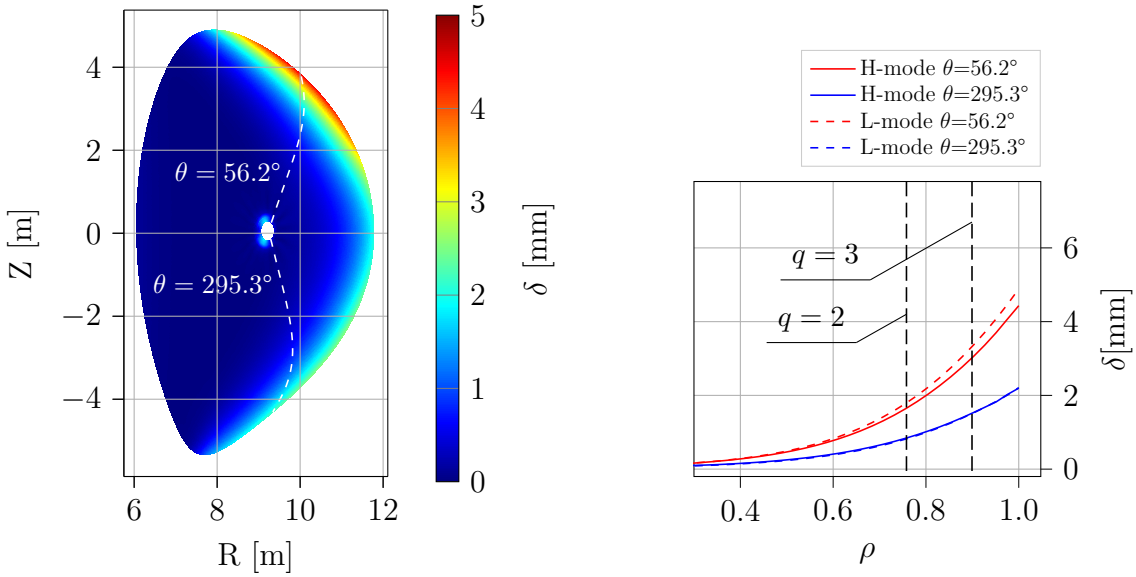

Figure 6.5: The amplitude of the flux surface corrugation $\delta(R, Z)$ (eq. (2.14)) of the H-mode in the vacuum induction field with ferromagnetic inserts. The same scenario is computed figure 6.4 with a force tolerance `ftol`$=1 \cdot 10^{-11}$ in the NEMEC simulation. In this plot the force tolerance is lowered to `ftol`$=1 \cdot 10^{-14}$, while all other simulation parameters are unchanged to the corresponding case in figure 6.4. This reduction of the force tolerance enforces NEMEC to compute flux surfaces with a smaller residual equilibrium force. Thus, the fluctuation in δ, shown in figure 6.4, vanishes.

7 Conclusion and outlook

The conclusion of this work is oriented to the two major objectives, stated in the motivation in section 1.2.

- *Coupling of a code system for the computation of 3D flux surfaces in ideal MHD equilibrium.*

  Starting with output of ASTRA simulations, supplying

  - pressure profile,
  - plasma current profile,
  - poloidal flux,
  - initial boundary and magnetic axis

  for different plasma scenarios, the newly developed code PIGEN is used to preprocess the output to NEMEC simulations. This coupling of ASTRA to NEMEC is supplemented by 3D vacuum induction fields, with a finite number of toroidal field coils, offering the possibility for 3D free-boundary simulations in NEMEC. The vacuum fields are computed all over this work with MAKEGRID. For the parametric generation of MAKEGRID input files, of realistic coil systems, a code called MIGEN is developed. The parametric design of MIGEN accelerates the translation of different coil systems into MAKEGRID format. Besides the native coils (toroidal field coils, poloidal field coils and central solenoid) MIGEN implements the translation of ferromagnetic inserts inside the vacuum vessel wall into a coil model. This coil model is shown to reproduce the dependence of a filling factor of the volume qualitatively for all filling factors of the ferromagnetic inserts. For higher filling factors however, the coil model predicts a weaker overcompensation of the toroidal field ripple, compared to [11].
- *Compute plasma response to the toroidal field ripple for the latest DEMO baselines.*

  The plasma response, in terms of the amplitude of the flux surface corrugation $\delta(R, Z)$, to the toroidal field ripple is computed based on

  - the engineering parameters of DEMO baseline 2018,
  - the geometry of the toroidal field coils and the ferromagnetic inserts of DEMO baseline 2017 and
  - the geometry of the poloidal field coils and the central solenoid of DEMO baseline 2019.

  The results for the L-mode, investigated in this thesis, show the expected results, that the toroidal field ripple is a non-resonant perturbation. This is confirmed by showing direct translation of the toroidal field ripple into the flux surface corrugation. This conclusion is further confirmed for the H-mode, where a lower force tolerance is required in NEMEC

simulations. With this lower force tolerance it can be seen, that the amplitude of the flux surface corrugation is the same for L-mode and H-mode, as visualized in this thesis. Additionally, a comparison between vacuum approximation and a corresponding 3D free-boundary NEMEC simulation for the L-mode shows, that the vacuum approximation can not fully capture the plasma response to the toroidal field ripple.

At the end of the presented work an outlook, for potential progress in the future, based on this work, is given with the following points.

- Magnetic perturbations coils (MP coils) are non-axisymmetric coils for control purposes of the plasma. A routine inside MIGEN for the creation of MP coils is not implemented at the moment and would complete the 3D coil system. This would offer the possibility to include further 3D perturbations inside NEMEC simulations.
- For the applicability of the developed coil model for ferromagnetic inserts the coil current computation can be improved. As presented in this work the dependence of the filling factor in the coil current computation is qualitatively as expected. However, for filling factors near 100 % a weaker overcompensation of the toroidal field ripple than in [11] is computed. It is observed within this work, that the geometry of the ferromagnetic insert coils can reproduce the results [11] quantitatively by adjusting the coil currents manually (figure 5.12). Therefore, the major sources of uncertainties are the extrapolation of the magnetic permeability curve and the implementation of the filling factor.

Bibliography

[1] EUROfusion-Konsortium. Das Demonstrationskraftwerk DEMO. https://www.euro-fusion.org/de/programm/demo/, 2018. [last checked 04.03.2022].

[2] K. Miyamoto et al. *Plasma physics for controlled fusion*, volume 92. Springer, 2016.

[3] EUROfusion-Konsortium. EUROfusion Roadmap. https://www.euro-fusion.org/de/ueber-eurofusion/roadmap/, 2018. [last checked 09.02.2022].

[4] J.P. Freidberg. *Ideal MHD*. Cambridge University Press, 2014.

[5] E. Strumberger, S. Günter, E. Schwarz, C. Tichmann, et al. Fast particle losses due to NTMs and magnetic field ripple. *New Journal of Physics*, **10**(2):023017, 2008.

[6] A. Fasoli, C.B.H.L. Gormenzano, H.L. Berk, B. Breizman, S. Briguglio, D.S. Darrow, N. Gorelenkov, W.W. Heidbrink, A. Jaun, S.V. Konovalov, et al. Physics of energetic ions. *Nuclear Fusion*, **47**(6):S264, 2007.

[7] F. Schwabl. *Statistische Mechanik*. Springer, 2006.

[8] M. Kaufmann. *Plasmaphysik und Fusionsforschung*. Springer, 2013.

[9] M.D. Kruskal and R.M. Kulsrud. Equilibrium of a magnetically confined plasma in a toroid. *The Physics of Fluids*, **1**(4):265–274, 1958.

[10] W.D. D'haeseleer, W.N.G. Hitchon, J.D. Callen, and J.L. Shohet. *Flux coordinates and magnetic field structure: a guide to a fundamental tool of plasma theory*. Springer Science & Business Media, 2012.

[11] F. Villone, G. Rubinacci, and CREATE Team. Report on the 2019 3D EM model and Vertical Stability (VS) Analysis Report on 3D Electromagnetic analysis of DEMO disruptions. *Garching bei München: Max-Planck-Insitut für Plasmaphysik*, Report IDM reference No. EFDA_D_2MUNQ3, 2019.

[12] G. Suárez López. *Effect of non-axisymmetric tokamak plasmas on the coupling performance of ion cyclotron wave antennas*. PhD thesis, LMU, 2020.

[13] M. Schmidtmayr, J.W. Hughes, F. Ryter, E. Wolfrum, N. Cao, A.J. Creely, N. Howard, A.E. Hubbard, Y. Lin, M.L. Reinke, et al. Investigation of the critical edge ion heat flux for LH transitions in Alcator C-Mod and its dependence on BT. *Nuclear Fusion*, **58**(5): 056003, 2018.

[14] G. Suárez López. On the feasibility of the L-H transition for a purely electron heated EU-DEMO tokamak. *Not yet published*, 2022.

[15] P.A. Schneider, E. Wolfrum, R.J. Groebner, T.H. Osborne, M.N.A. Beurskens, M.G. Dunne, B. Kurzan, T. Pütterich, E. Viezzer, JET EFDA Contributors, et al. Analysis of temperature and density pedestal gradients in AUG, DIII-D and JET. *Nuclear Fusion*, **53**(7):073039, 2013.

[16] G.V. Pereverzev and P.N. Yushmanov. ASTRA. Automated System for TRansport Analysis in a tokamak. *Garching bei München: Max-Planck-Insitut für Plasmaphysik*, tech. rep.5/98, 2002.

[17] G.M. Staebler, J.E. Kinsey, and R.E. Waltz. Gyro-Landau fluid equations for trapped and passing particles. *Physics of Plasmas*, **12**(10):102508, 2005.

[18] G.M. Staebler, N.T. Howard, J. Candy, and C. Holland. A model of the saturation of coupled electron and ion scale gyrokinetic turbulence. *Nuclear Fusion*, **57**(6):066046, 2017.

[19] G.M. Staebler, J. Candy, E.A. Belli, J.E. Kinsey, N. Bonanomi, and B. Patel. Geometry dependence of the fluctuation intensity in gyrokinetic turbulence. *Plasma Physics and Controlled Fusion*, **63**(1):015013, 2020.

[20] E. Fable, C. Angioni, F.J. Casson, D. Told, A.A. Ivanov, F. Jenko, R.M. McDermott, S.Y. Medvedev, G.V. Pereverzev, F. Ryter, et al. Novel free-boundary equilibrium and transport solver with theory-based models and its validation against ASDEX Upgrade current ramp scenarios. *Plasma Physics and Controlled Fusion*, **55**(12):124028, 2013.

[21] A.A. Ivanov, R.R. Khayrutdinov, S.Y. Medvedev, Y.Y. Poshekhonov, et al. New adaptive grid plasma evolution code SPIDER. In *Proceedings of 32nd EPS Conference on Plasma Phys., Tarragona, 27 June–1 July 2005 ECA*, volume **29**, pages 5–063. Citeseer, 2005.

[22] D.E. Bernholdt and R. Whitfield. ORNL-Fusion. https://github.com/ORNL-Fusion, 2021. [last checked 27.08.2021].

[23] S.P. Hirshman and H.K. Meier. Optimized Fourier representations for three-dimensional magnetic surfaces. *The Physics of fluids*, **28**(5):1387–1391, 1985.

[24] P.E. Gill, W. Murray, and M.H. Wright. *Practical optimization*. SIAM, 2019.

[25] S.P. Hirshman and J.C. Whitson. Steepest-descent moment method for three-dimensional magnetohydrodynamic equilibria. *The Physics of fluids*, **26**(12):3553–3568, 1983.

[26] S.P. Hirshman and D.K. Lee. MOMCON: A spectral code for obtaining three-dimensional magnetohydrodynamic equilibria. *Computer physics communications*, **39**(2):161–172, 1986.

[27] S.P. Hirshman, P. Merkel, et al. Three-dimensional free boundary calculations using a spectral Green's function method. *Computer Physics Communications*, **43**(1):143–155, 1986.

[28] M. Siccinio, E. Fable, C. Angioni, S. Saarelma, A. Scarabosio, and H. Zohm. Impact of an integrated core/SOL description on the R and BT optimization of tokamak fusion reactors. *Nuclear Fusion*, **58**(1):016032, 2018.

[29] T.C. Luce. An analytic functional form for characterization and generation of axisymmetric plasma boundaries. *Plasma physics and controlled fusion*, **55**(9):095009, 2013.

[30] W. Nolting. Elektrodynamik. In *Grundkurs Theoretische Physik 3*. Springer, 2013.

[31] E. Strumberger, P. Merkel, E. Schwarz, and C. Tichmann. MFBE_2001:Computation of magnetic fields of ideal MHD equilibria. *Garching bei München: Max-Planck-Insitut für Plasmaphysik*, IPP report 5/100, 2002.

Danksagung

I'm grateful for the guidance into fusion research, that was provided to me by my supervisors from Max-Planck-Institute for Plasma Physics Prof. Dr. Hartmut Zohm and Dr. Guilermo Suárez López. I enjoyed their patience, comprehensive knowledge in plasma physics and their delight, while solving complex problems. They always supported me with profound insights to fusion research in a didactically valuable manner.

Furthermore, I would like to thank Prof. Dr. Gerd Ganteför for enabling me the possibility, to work on a topic that I'm interested in for years. His cheerful nature always inspired me.

I would like also to thank all members of the Max-Planck-Institute for Plasma Physics who developed codes that I could fall back on. Especially the preceding effort of my supervisor Dr. Guilermo Suárez López in creating parallelized codes accelerated my work significantly.

Without the financial and mental support of my family and my friends it would not have been possible for me, to finish this thesis and moreover my Master program in general. Especially Sandra, who has been with me through many exhausting years, always supported me with her patience and her trust in me. Thank you.